Accurate simulation of the noise generated by a hot supersonic jet including turbulence tripping and nonlinear acoustic propagation F

Adrien Langenais (iD), François Vuillot, Julien Troyes, and Christophe Bailly (iD)

COLLECTIONS

F   This paper was selected as Featured

View Online   Export Citation   CrossMark

ARTICLES YOU MAY BE INTERESTED IN

Researchers accurately simulate noise created by supersonic jets
Scilight **2019**, 050007 (2019); https://doi.org/10.1063/1.5090497

Sound radiation by supersonic unstable modes in hypersonic blunt cone boundary layers. I. Linear stability theory
Physics of Fluids **31**, 024103 (2019); https://doi.org/10.1063/1.5055761

Smoothed particle hydrodynamics (SPH) for complex fluid flows: Recent developments in methodology and applications
Physics of Fluids **31**, 011301 (2019); https://doi.org/10.1063/1.5068697

Accurate simulation of the noise generated by a hot supersonic jet including turbulence tripping and nonlinear acoustic propagation ⓕ ⓢⓒⓘ

View Online　　Export Citation　　CrossMark

Adrien Langenais,[1,a] ⓘⒹ François Vuillot,[1,b] Julien Troyes,[2,c] and Christophe Bailly[3,d] ⓘⒹ

AFFILIATIONS

[1] DMPE, ONERA, University of Paris-Saclay, Palaiseau, France

[2] DMPE, ONERA, University of Toulouse, Toulouse, France

[3] LMFA, UMR CNRS 5509, École Centrale de Lyon, University of Lyon, Écully, France

[a] Electronic mail: adrien.langenais@onera.fr
[b] Electronic mail: francois.vuillot@onera.fr
[c] Electronic mail: julien.troyes@onera.fr
[d] Electronic mail: christophe.bailly@ec-lyon.fr

ABSTRACT

A procedure to accurately simulate a free hot supersonic jet and its associated noise, which uses simultaneously a turbulence tripping method and a two-way coupling between a flow solver and a nonlinear acoustic solver, is proposed in this study. A Mach 3.1 overexpanded hot jet is computed via a large-eddy simulation by solving the filtered Navier-Stokes equations with a finite volume method on unstructured grids. The resulting noise is propagated in the far field by solving the full Euler equations with a high-order discontinuous Galerkin method on unstructured grids. The full convergent-divergent nozzle is explicitly included in the computational domain thanks to the unstructured flow solver. Both a refined grid and a geometrical boundary layer tripping in the convergent are used to get highly disturbed turbulent conditions at the nozzle lips. The flow field appears to agree with the expected turbulence behavior and the available experimental data. The jet development shows significant improvement compared to similar past simulations. The far field acoustic levels are finely recovered at most of the observation angles. An analysis of the acoustic near and far fields is then performed. The studied conditions lead to strong shock-associated noise and Mach wave emission. The spatio-frequency and azimuthal content of the acoustic field are described in order to identify the main noise properties. A particular noise component, different from screech tones and radiating upstream like Mach waves, is highlighted. Nonlinear propagation effects are finally quantified through specific metrics. They are found to be significant in both the near and the far fields, which justifies the use of a nonlinear acoustic solver.

I. INTRODUCTION

Understanding and controlling the noise radiated by rocket engine jets at lift-off is a major issue for space applications. Imperfectly expanded hot supersonic jets are generated and deflected in a flame trench at lift-off, generating a harsh acoustic field which induces severe loads on the launcher, the payload, and the surrounding structures.[1] Since the founding work of Lighthill, supersonic

jet noise has been carefully investigated, as extensively reviewed by Tam[2] or Bailly and Fujii.[3] Experimental studies have first been conducted to identify noise sources as reported by Tam *et al.*[4] for instance. Based on measured data, three main components have been highlighted: the turbulent mixing noise, the broadband shock-associated noise (BBSAN), and the Mach wave radiation. Numerous authors have contributed by studying specific mechanisms including nonlinearities and crackle,[5–8] screech and

feedback effects,[9–11] interaction with obstacles,[10,12] or with noise reduction devices.[13] Available experimental studies regarding imperfectly expanded hot supersonic jets at a Mach number $M > 3$ as proposed for example by Horne *et al.*[14] are, however, limited.

Semi-empirical noise sources and propagation models have been developed in parallel[15] but their ability to predict realistic installation effects remains poor. On the contrary, numerical simulations of the Navier-Stokes (NS) equations give access to detailed flow information on increasingly complex configurations.

The large-eddy simulation (LES) of a Mach 3.0 cold jet by Nonomura and Fujii[16] with focuses on overexpansion effects, and the simulation of Mach 1.3-1.5 planar and round cold jets by Gojon *et al.*[17] and Bogey and Gojon[18] with emphasis on feedback mechanisms, can be mentioned as advanced numerical studies. Imperfectly expanded hot supersonic jet computations have also been performed over the past decade. de Cacqueray and Bogey[19] have simulated a Mach 3.3 heated overexpanded free jet, investigating noise generation mechanisms. Brès *et al.*[20] have simulated a Mach 1.5 heated overexpanded free jet on various meshes, underlining the importance of addressing the boundary layer inside the nozzle and the turbulent state.

The jet initial conditions at the nozzle exit, especially the turbulence level close to the lips, have been found to be critical to perform high fidelity computations.[21–24] It has been observed experimentally that increasing the initial turbulence level expands the shear layer thickness[25] and its spread rate.[26] Long *et al.*[25] have also found that increasing the initial turbulence level leads to a reduction of the screech tones and of the shock-associated noise, suggesting a major influence of turbulence properties on the interaction mechanisms between turbulence and shocks. Fontaine *et al.*[27] have demonstrated that a thicker initial shear layer induces a significant noise reduction. Similar trends have been obtained numerically.[28] Liu *et al.*[22] have performed the simulation of underexpanded supersonic jets, explicitly including the nozzle geometry, and have also shown that the shear layer thickness increased when the initial turbulence level is raised from 1.2% to 7%. However, a minor impact on noise levels has been observed. On the contrary, the work by Bogey *et al.*[21] on a subsonic jet has demonstrated an important reduction of the noise overestimation when increasing the initial turbulence level from 0% to 12%. Main effects have appeared when moving from 0% to 3% and have been attributed to a weaker vortex pairing in the shear layer. Consequently, many computations now use a forcing strategy to mimic the incoming turbulent boundary layer. It consists in either a flow seeding with synthetic disturbances as performed by Bogey and Marsden,[28] Gloor *et al.*,[29] and Brès *et al.*,[24] for instance, or a geometrical tripping upstream of the nozzle exit as described by Liu *et al.*,[22] Lorteau *et al.*,[23] or Brès *et al.*[20] Mesh refinement, particularly in the azimuthal direction, is also admitted to be a key feature to accurately simulate supersonic jets and the generated noise by LES.[21,23,30]

The constantly increasing available computing resources allow even more accurate LES or direct flow computation. Including the whole acoustic field in such approaches, however, remains out of reach for realistic applications. The acoustic far field can be calculated by an integral acoustic formulation applied to a control surface,[31] such as the Kirchhoff or the Ffowcs Williams and Hawkings (FWH) integral methods. Nonlinear propagation effects induced by high sound pressure levels (SPL) in space applications, such as wave distortion, and installation effects linked to the launch pad geometry, are not readily taken into account by these approaches.

Coupling methods between flow and acoustic solvers have been evaluated and applied to jet noise. The Navier-Stokes equations are usually solved by LES and weakly coupled to the linearized Euler equations (LEEs),[32,33] that is, with no feedback from the acoustic region. More recently, de Cacqueray *et al.*[19,34] have simulated the noise emitted from a Mach 3.3 jet with a one-way Navier-Stokes-Euler coupling using a high-order structured solver. An analysis of far field noise components and a quantification of nonlinear propagation effects have been conducted. Harris *et al.*[35,36] have overlapped an unstructured LES and a discontinuous Galerkin acoustic solver to run a 2D simulation of the Space Launch System acoustic environment. Labbé *et al.*[37] have performed a one-way Navier-Stokes-Euler coupling for subsonic jet noise prediction. Results have been compared to those obtained from the Ffowcs Williams and Hawkings integral method and have agreed in the linear regime as expected. Tsutsumi *et al.*[38] have applied a one-way Navier-Stokes-Euler coupling to a reduced scale flame trench, showing the ability of the method to treat realistic launch pad configurations. Space applications may imply complex secondary flows and acoustic feedback on the primary flow which can be taken into account only with a two-way method. Two-way coupling between fully 3D unstructured Navier-Stokes and Euler solvers has been recently developed and validated for space applications.[39]

Finally, the presence of acoustic nonlinearities in the near field is admitted,[6,40] but the need of a nonlinear acoustic solver to compute the far field propagation is still debated. The dimensionless Goldberg number Γ can be introduced[7] as an indicator to distinguish regions where cumulative acoustic nonlinearities are dominant compared to the atmospheric damping. The noise levels observed in space applications suggest that significant cumulative nonlinearities occur in the far field, resulting in waveform steepening, shock coalescence, and amplitude loss compared to linear propagation.[41,42] Specific metrics have been proposed and assessed to quantify the nonlinear propagation, especially, the pressure derivative skewness, the pressure derivative kurtosis, and the wave steepening factor (WSF).[7,8,43] de Cacqueray and Bogey[19] have compared the far field propagation of the noise generated by a Mach 3.3 jet computed with the linearized and the full Euler equations. The LEE simulation has resulted in a 5 dB noise overestimation at 120D in the peak direction. Similar trends have been observed by comparing Ffowcs Williams and

Hawkings and full Euler computations.[44] The FWH method overestimates the far field noise by about 2 dB at 40D in the peak direction. These pieces of evidence clearly indicate that nonlinear propagation effects cannot be ignored in the far field.

In the present work, a free hot supersonic jet at a Mach number of 3.1 is simulated using simultaneously a turbulence tripping method and a two-way coupling between unstructured flow and acoustic solvers. The solvers are based on the Navier-Stokes equations written for LES and solved by a finite volume method and the full Euler equations solved by a high-order discontinuous Galerkin method, respectively. The study is organized in three main parts. First, the simulation methodology is described in Sec. II. The main jet properties, the comparison database, and the numerical setup are detailed in Sec. II A. The numerical tools are presented in Sec. II B. Then, major grid effects are discussed in Sec. II C. A geometrical turbulence tripping method is implemented in Sec. II D. The resulting flow inside the nozzle is also described. Second, the free jet flow computation and the resulting noise are carefully validated in Sec. III by comparing results to available experimental and numerical data. Sections III A and III B are dedicated to aerodynamic and acoustic validation, respectively. Third, main noise sources and acoustic propagation phenomena are analyzed in Sec. IV. The noise sources are discussed *a priori* and linked to the computed acoustic field in Sec. IV A. The properties of the velocity and pressure near fields and of the pressure far field are characterized in Secs. IV B and IV C, respectively. Finally, the nonlinear acoustic propagation effects are highlighted and quantified in Sec. IV D. Concluding remarks are given in Sec. V.

II. SIMULATION METHODOLOGY

A. Jet case setup and database

1. Physical parameters and notations

An overexpanded hot jet with an exit Mach number $M_j = u_j/c_j = 3.1$ and a Reynolds number $Re_D = u_j D/\nu_j = 3 \times 10^5$ is considered, where the subscript j refers to the jet conditions on the centerline in the nozzle exit plane, u refers to the velocity, c refers to the speed of sound, D refers to the diameter, and ν refers to the kinematic viscosity. The corresponding ideally expanded Mach number is $M_d = 2.8$. The jet fluid is composed of an equivalent propellant gas resulting from a hydrogen-air combustion. The specific heat ratio is $\gamma = 1.3$. The generating conditions are $p_i = 30 \times 10^5$ Pa for the total pressure and $T_i = 1900$ K for the total temperature. The jet is exhausted from a convergent-divergent nozzle with an exit diameter $D = 60$ mm, under conditions $T_j/T_\infty = 2.6$ and $p_j/p_\infty = 0.6$. Ambient medium is air at $\gamma = 1.4$, $T = T_\infty = 293.15$ K, and $p = p_\infty = 1 \times 10^5$ Pa. The main flow parameters are recalled in Table I. The generated noise reaches very high acoustic levels typically greater than 130 dB out to 40D from the sources. In the following, all positions and length quantities referred by the superscript $*$ are made dimensionless

TABLE I. Studied supersonic jet operating conditions.

M_j	M_d	p_j/p_∞	T_i/T_∞	$Re_D \times 10^{-6}$	D	D_j
3.1	2.8	0.6	6.5	0.3	60 mm	0.97D

by the jet exit diameter D_j. All dB scales are calculated with a reference value of 2×10^{-5} SI.

2. Experimental and numerical database

The present jet parameters correspond to those of an experimental study conducted at the same scale in the MARTEL semi-anechoic facility. The hydrogen-air combustion provides generating conditions in the range $p_i = 25 - 30 \times 10^5$ Pa, $T_i = 500 - 2100$ K, and a maximum overexpanded exit velocity of 1800 m/s. The test bench aims at investigating supersonic, free, or impinging jet noise under launcher lift-off conditions from a reduced scale motor (about 1/40 based on the Ariane 5 solid propellant boosters). The experimental setup for the considered case is depicted in Fig. 1(a). Two-component laser Doppler velocimetry (LDV) and far field acoustic measurements have been carried out. Measurements include axial and radial profiles of mean axial $\overline{u}_x$ and radial $\overline{u}_r$ velocities, root mean square (RMS) fluctuating axial u'_x and radial u'_r velocities, axial velocity skewness $S(u_x)$ and kurtosis $K(u_x)$, along the jet axis and along four radii positioned at $x_* = x/D_j = 1, 3, 3.67,$ and 6. A microphone arc of radius 41.6D, centered on the nozzle exit, provides far field acoustic measurements. The wedges aim at isolating microphones from reflected waves by the ground and the small central region without wedges is not expected to contribute to recorded signals [Fig. 1(a) not at scale]. Microphones are spaced every $\Delta\theta = 10°$ and their frequency bandwidth is 50 kHz.

LESs of the same free jet have first been performed by Troyes *et al.*[45] The acoustic far field was computed with the Ffowcs Williams and Hawkings method.[31] More recently, Langenais *et al.*[44] have adapted the case by using an identical near field mesh and computing the far field with the full Euler equations. Resulting aerodynamic and acoustic fields provide a valuable numerical database which will be referred to as Langenais 2017[44] in the following.

3. Computational setup

In the present numerical investigation, the jet and the acoustic near field are simulated by solving the Navier-Stokes equations by LES in the region hereafter denoted as Z1 and the acoustic far field is computed solving the full Euler equations in the region Z2, as illustrated in Fig. 1(b). The two solvers exchange data at a conical coupling interface S1. The origin of the coordinate system is located at the nozzle exit plane on the jet axis. The cylindrical coordinate system (x, r, Θ) centered on the jet axis is preferred for analysis convenience. The full convergent-divergent nozzle geometry is explicitly included in the domain. Qualitatively based on a previous flow solution,[44] the coupling interface radius is chosen as
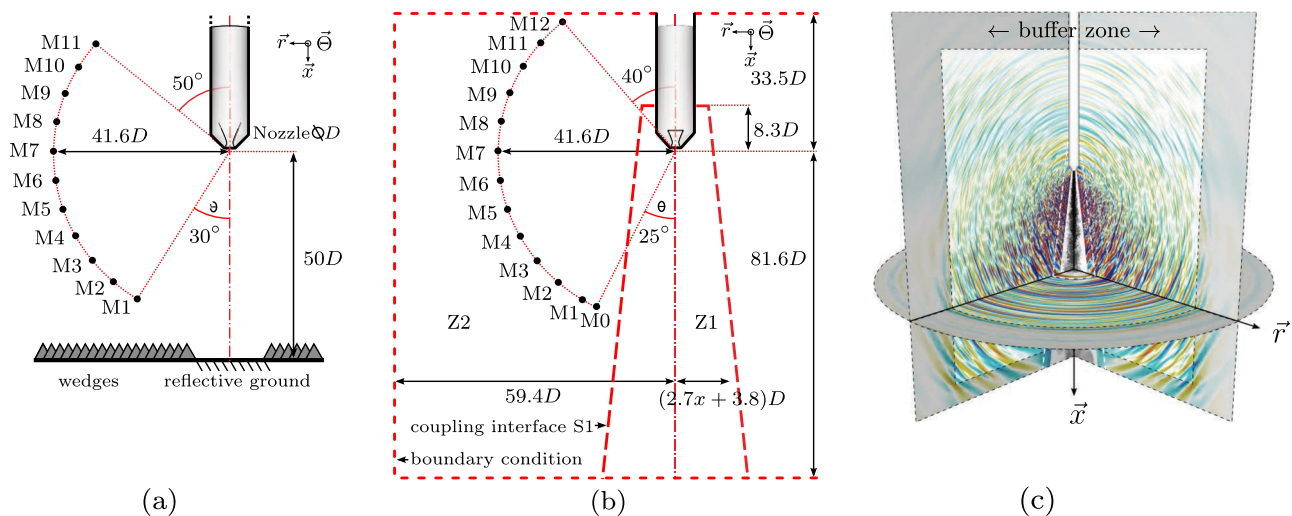
FIG. 1. Dimensions of (a) the experimental setup at the MARTEL facility and (b) the present computational setup; (c) visualization of the 3D numerical domain.

$r = (2.7x + 3.8)D$ in order to follow the jet expansion. The ground is not included in the domain which extends $33.5D$ upstream, $81.6D$ downstream, and $59.4D$ laterally. In addition to the surrounding buffer zone depicted in Fig. 1(c) where the grid is stretched, a characteristic-based non-reflective condition[46] is set at the domain boundary in the zone Z2 and a standard outflow condition with an imposed pressure $p = p_\infty$ is set downstream in the zone Z1. Finally, far field recording points are placed at the experimental microphone locations in the zone Z2, as well as at the LDV measurement locations in the zone Z1.

The main computation has been performed on 1736 Broadwell processors of the ONERA's parallel scalar cluster SATOR, including 1512 cores allocated to the Navier-Stokes solver and 224 cores allocated to the Euler solver. A total physical time of 1180 D/u_j has been simulated, which provides a fully established state duration of 650 $D/u_j = 130$ D/c_∞ as exploitable time. It is comparable to similar computations in the literature[19,20] but can be limited in terms of temporal convergence for low frequencies. The minimum accessible frequency is $St_{min} = 1.5 \times 10^{-3}$, but, in practice, a relevant low frequency bound considering at least five periods is $St_{min} = 8 \times 10^{-3}$. The total computational cost is 4.5×10^6 CPUh.

B. Numerical methods and settings

1. Flow computation

The ONERA multi-physics code CEDRE which operates on general unstructured elements[47] is used in the zone Z1. The filtered compressible Navier-Stokes equations are solved with a Smagorinsky subgrid scale model with a constant value $C_s = 0.1$. No wall model is used, but the van Driest damping function is implemented. The specific heat is defined by a 7th order polynomial for air and is set constant for the propellant

gas. Species viscosity is calculated according to the Sutherland law. The time integration is performed with an implicit 2nd order Runge-Kutta scheme associated with a Gemeralized Minimal RESidual (GMRES) method type linear system solver. The flux calculation is carried out with a 2nd order Monotonic Upwind Scheme for Conservation Laws (MUSCL) method and a Harten-Lax-van Leer-Contact (HLLC) flux scheme. The required spatial discretization is characterized in terms of point per wavelength (PPW). This criterion is linked to the computation cut-off Strouhal number as

$$St_c = \frac{f_c D_j}{u_j} = \frac{c_\infty D_j}{\lambda_c u_j} = \frac{c_\infty D_j}{(PPW \times K \times \Delta)u_j}, \quad (1)$$

where f_c is the cut-off frequency, λ_c is the cut-off wavelength, Δ is the grid characteristic size, and K is a correction constant. Based on preliminary computations and previous studies, the K parameter is set to 1.2 to match the prediction with the observed cut-off frequency. The setting of Δ is discussed in Sec. II C 2 dealing with the grid parameters. A resolution of PPW = 20 has been found to be required for a proper acoustic propagation in the near field with the CEDRE code.[45] The associated numerical damping reaches its maximum value of 0.5 dB/λ_c at the cutoff.

2. Acoustic computation

The ONERA unstructured computational aeroacoustics (CAA) code SPACE[48,49] is used in the zone Z2. The full Euler equations are solved through a nodal discontinuous Galerkin method using high-order polynomial elements without order limit. The thermodynamic properties of the propagation medium (air) are set constant with $\gamma = 1.4$. The time integration is performed with an explicit 2nd order Runge-Kutta scheme, and high spatial orders up to the 4th order are used. It has been established that high-order methods for aeroacoustic problems are beneficial in terms of cost/accuracy ratio.[50]

According to Delorme et al.,[48] a PPW = 14 discretization is required at the 2nd spatial order and only PPW = 3 at the 4th order for an ideal case of wave propagation. The cut-off Strouhal number is linked to PPW via Eq. (1), and K is set to 1.2 as previously. A higher resolution of PPW = 5 at the 4th order is chosen here. The resulting numerical dissipation is of the order of the atmospheric viscous damping, i.e., $\sim10^{-3}$ dB/λ over the resolved spectrum.[51] The discontinuous Galerkin method implemented in SPACE also allows the user to locally adapt the spatial orders. This method is called order mapping or p-adaptation and greatly improves the usage convenience. A description of the non-reflective boundary conditions and the shock-capturing scheme can be found in Langenais et al.[39]

3. Two-way coupling

The flow and the acoustic solvers are linked through a two-way surfacic coupling. Cell location, data exchange, and space interpolation are carried out with the Coupling With Interpolation Parallel Interface (CWIPI) coupling library[47,52] via Message Passing Interface (MPI) communications. No mesh overlapping is used at the coupling interface. The same space discretization is considered at the interface in both solvers, i.e., conformal tetrahedral meshes. The coupling algorithm consists in locating the boundary cells on each side of the interface, then calculating, and exchanging the values required by the other code at cell centers for CEDRE and nodes for SPACE, at every time step. Note that the use of conformal grids and the exchange at every time step increase the coupling robustness and allow us to minimize the signal degradation which could be induced by spatial or temporal aliasing. However, it implies additional constraints such as the same time step in both solvers. The values of the conservative variables sent to SPACE are calculated from CEDRE primitive values (p, T, $\mathbf{u}$) with SPACE thermodynamic laws. Multi-species LESs can therefore be carried out without pressure, temperature, or velocity discontinuities across the interface. At the end of a coupling cycle, exchanged values are used by each solver to compute the numerical flux at the interface. An extended description of the coupling features and a set of appropriated validation test cases can be found in Langenais et al.[39]

Since the flow and the acoustic computations are second and fourth order accurate, respectively, the coupling interface can be seen as an accuracy discontinuity which could generate numerical instabilities. This issue is treated by locally adapting the element order close to the interface on the SPACE side. The small-sized cells induced by the conformal meshes at the interface are set to the second order. Moving away from the interface, the cell size increases and the element order quickly rises to the third order and finally, to the fourth order. This method provides a smooth transition in terms of numerical accuracy without reducing the global computation order since the flow solution remains second order accurate.

The fully unstructured coupling methodology is able to deal with complex geometries and acoustic feedback on the flow. In the present free jet case, the benefits of these features mainly lie in the ability to easily mesh the nozzle and to take into account the induced secondary flow given that no acoustic feedback is expected.

C. Grid effects

1. Past efforts

A common supersonic nozzle used in a series of MARTEL test campaigns (see Sec. II A 2) has formed the basis of several sets of LES computations at ONERA aiming at predicting the acoustic far field. Troyes et al. have simulated jet cases corresponding to experiments conducted at the MARTEL test bench.[45] Major grid effects have been investigated. A sufficiently refined unstructured mesh has been found to be required on the jet axis to accurately capture shock cell locations. The azimuthal resolution at the nozzle lips has been found to significantly influence the early shear layer development. More recently, the far field mesh of the same free jet case[45] has been adapted by Langenais et al.[44] to perform a Navier-Stokes-Euler coupled computation following the procedure described in Sec. II B 3. Since the near field mesh and flow solution were unchanged, it has allowed us to specifically study the impact of the nonlinearities on the acoustic far field. This work has also concluded that further mesh refinement was needed to better resolve the jet flow solution, especially, the early jet development.

2. Present improvement

The present work involves a refined mesh described in the current section and a geometrical turbulence tripping method consisting in a small step added at the nozzle wall as discussed in Sec. II D.

The grid is unstructured and mainly composed of tetrahedra. The refinement effort is focused on the nozzle wall, the lips, the shear layer, and the first two shock cell centerline regions. The motor body and the nozzle wall are meshed with a dozen of hexahedral layers. The cell sizes are reported in Table II at key locations in terms of axial, azimuthal, and radial characteristic lengths for the hexahedra and characteristic edge for the tetrahedra. The corresponding equivalent cell diameter d_{cell} is chosen as characteristic grid size Δ and is given by

$$d_{cell} = \Delta = \frac{6V}{A} \simeq \frac{\sqrt{6}}{6}e,\tag{2}$$

where A is the cell faces total area, V is the cell volume, and e is the tetrahedron edge. Note that d_{cell} is strictly equal to $(\sqrt{6}/6)e$ only in the case of a regular tetrahedron. The hexahedral layers in the nozzle are not refined enough to fully resolve the boundary layer ($y^+ \simeq 12$ at the nozzle throat and $y^+ \simeq 10$ at the separation point) but enough to convect the forced velocity fluctuations as part of the turbulence tripping method discussed in Sec. II D. The hexahedra at the nozzle lips provide an azimuthal resolution of about $2\pi/\Delta\theta \simeq 1300$ cells which is nearly three times the resolution of the previous grid.[44] The axial variation of d_{cell} inside the nozzle boundary layer and along the lipline in the shear layer is plotted in Fig. 2. The drop at $x = 0$ can be explained by the transition between

TABLE II. Cell characteristic size at key locations.

Element								Hexahedra								
Zone	Nozzle step				Nozzle throat				Nozzle divergent				Nozzle lips			
Axial location $\times D^{-1}$	-1.37				-1.16				-0.17				-0			
Characteristic length	Δx	$r\Delta\theta$	Δr	d_{cell}	Δx	$r\Delta\theta$	Δr	d_{cell}	Δx	$r\Delta\theta$	Δr	d_{cell}	Δx	$r\Delta\theta$	Δr	d_{cell}
Size $\times 10^3\ D^{-1}$	1.2	1.3	1.0	1.2	1.0	1.0	0.6	0.8	1.7	2.2	1.4	1.7	1.5	2.4	1.4	1.7

Element					Tetrahedra						
Zone	Lips		Shear layer		Jet axis				NS acou. field		Euler acou. field	
Axial location $\times D^{-1}$	0		1		0		1.33		. . .		. . .	
Characteristic length	e	d_{cell}	e	d_{cell}	e	d_{cell}	e	d_{cell}	e	d_{cell}	e	d_{cell}
Size $\times 10^3\ D^{-1}$	1.7	0.7	6.7	2.7	13.3	5.4	11.7	4.8	66.7	27.2	367	150

hexahedral and tetrahedral elements. Downstream, the tetra-hedron stretching is nearly linear and the stretching rate tends to d(d_{cell})/dx = 0.001 which is two orders of magnitude lower than a representative shear layer spread rate for such a super-sonic jet.[26] It should enable a proper development of the shear layer and a good resolution of the turbulent spectra. The cell size indicated for the Navier-Stokes acoustic field in Table II is maintained up to x = 20D. Downstream, the mesh is slowly coarsened by doubling the cell size in the range 20D < x < 42D. The cell size indicated for the Euler acoustic field is maintained up to x = −28D upstream, x = 42D down-stream, and r = 42D laterally. According to Eq. (1) and d_{cell} values reported in Table II, the cut-off frequencies of the Navier-Stokes acoustic field (x ≤ 20D) are St_c = 0.30 consider-ing PPW = 20 (see Sec. II B 1) which is slightly overrated for the acoustics because of the aerodynamics. The cut-off frequen-cies of the Euler acoustic field are St_c = 0.22 considering PPW = 5 (see Sec. II B 2), while the cut-off frequency of the previous computation was St_c = 0.15.[44] The entire mesh is composed of
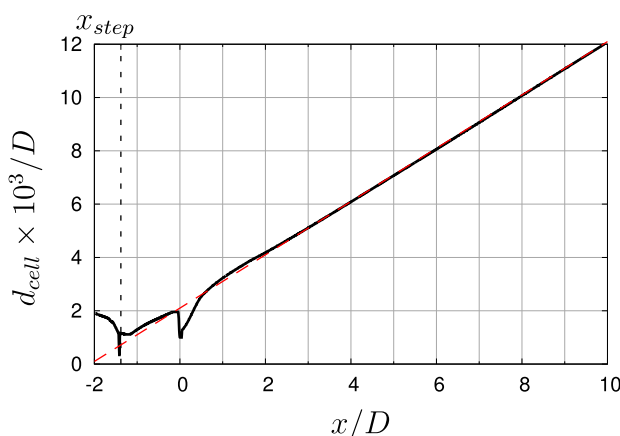

FIG. 2. Characteristic cell diameter d_{cell} in the nozzle wall boundary layer and the shear layer. Black solid line: mesh and red dashed line: asymptotic stretching rate d(d_{cell})/dx = 0.001.

290×10^6 cells including 235×10^6 cells in Z1 and 55×10^6 cells in Z2.

D. Turbulence tripping

1. Tripping strategy

The previous computation of the present free jet case[44] has shown a lack of turbulent fluctuations in the shear layer at $x_* = 1$ in regard to the experimental levels. It has resulted in a too rapid laminar-turbulent transition, a too strong vortex pairing, and a significant noise overestimation at mid frequen-cies. As examined previously in the Introduction, numerical simulations at a high Reynolds number require a forcing strat-egy to trigger the transition from a laminar to a turbulent state.[28] The chosen approach here consists in a geometrical tripping as implemented in other existing studies. Liu et al.[53] have added a sawtooth surface roughness in the convergent of a supersonic nozzle. The roughness height is 1% of the noz-zle diameter and enables a 5% turbulence level increase at the nozzle lips. Lorteau et al.[23] have used a rectangular step in a converging subsonic nozzle. The step height is 0.5% of the nozzle diameter, and the shape is axisymmetric to avoid spurious azimuthal mode excitation.

In the present tripping strategy, an axisymmetric step is added at the nozzle wall at an axial location x_{step}. A para-metric study is carried out to optimize the tripping benefit, as summarized in Sec. II D 2. The resulting wall flow inside the nozzle is described in Sec. II D 3 in the case of the full computation.

2. Parametric study

The parametric study is conducted by varying the step main parameters, i.e., the axial location x_{step}, the height h, and the top edge slope. Five step configurations have been investi-gated, named steps A, B, C, D, and without step, on a reduced computational domain. The detailed configurations and pro-cedure are provided in the Appendix. The step C located in the convergent, with parameters x_{step} = −1.38D, h = 0.01D, and the edge slope parallel to the axis $\vec{x}$, is implemented in the
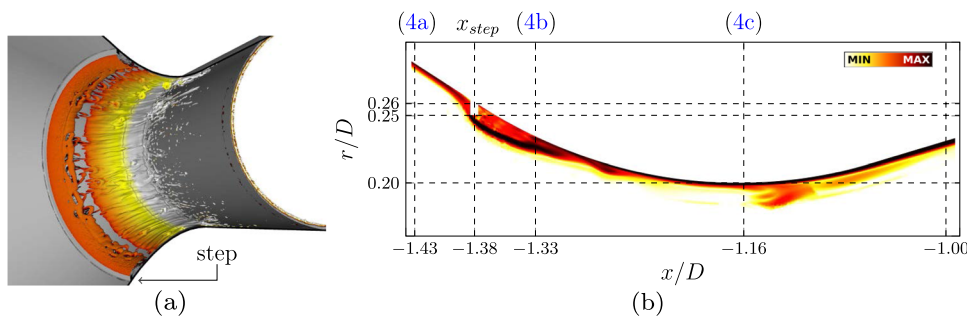
FIG. 3. Flow snapshots in the vicinity of the step. (a) Visualization of iso-Q-criterion surfaces colored by the velocity magnitude and (b) 2D visualization of the vorticity intensity.

full computation. It provides a highly disturbed flow close to the nozzle lips with fluctuation levels $u'/u_j > 3\%$, while the configuration without step leads to $u'/u_j < 0.5\%$ on a comparable grid. The full mesh in the zone Z1 finally includes 235×10^6 cells, which adds 17.7×10^6 cells compared to the base without trip.

3. Nozzle wall flow

Figures 3 and 4 show the snapshots of the Q-criterion [Fig. 3(a)] and vorticity [Figs. 3(b) and 4] inside the nozzle.

The effect of the step C is clearly visible. A separated flow and a recirculation zone of length $\approx 4h$ are generated above and immediately downstream of the step, as it can be seen on the mean velocity profiles in Fig. 5(a). Vortical structures and velocity fluctuations are generated and convected downstream within the boundary layer. Axial velocity fluctuations reach important root mean square levels up to about 15% of the mean velocity on the axis, as shown in Fig. 5(b). This figure also illustrates the mesh discretization near the wall. The power spectral density (PSD) of the velocity fluctuations
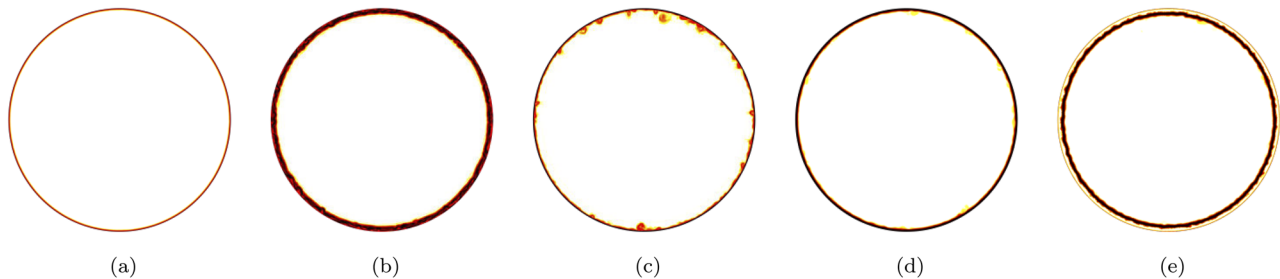
FIG. 4. Dimensionless transversal cut of vorticity in the nozzle at various axial locations. (a) $x = -1.43D$, (b) $x = -1.33D$, (c) $x = -1.16D$, (d) $x = -0.50D$, and (e) $x = 0D$.
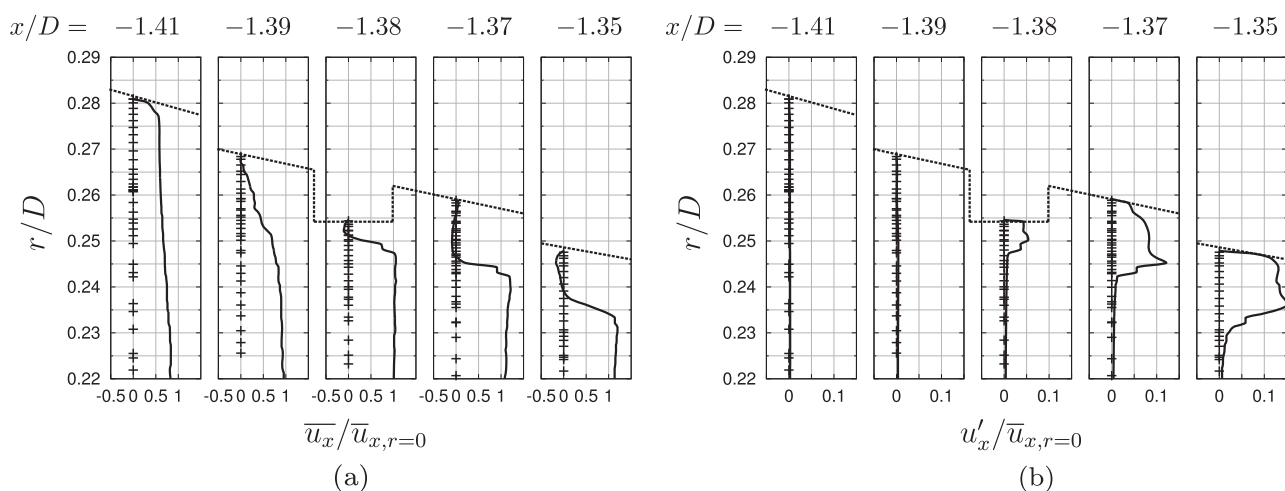

FIG. 5. Velocity properties in the vicinity of the step. (a) Mean axial velocity and (b) fluctuating axial velocity. Black solid line: numerical data; black dashed line: nozzle wall, and black plused: unstructured mesh discretization every 2 points.

immediately downstream of the step (not plotted) appears to be broadband centered on $St_{step} = fh/u_0 \sim 0.01$, where u_0 is the mean velocity outside the boundary layer above the step. The generated structures are then strongly stretched at the throat and in the divergent which can be associated with a relaminarization phenomenon, as expected for such highly accelerated compressible flow.[54] A similar stretching has been observed by Liu *et al.*[53] for their supersonic jet simulation also using a geometrical turbulence tripping.

The main boundary layer properties are depicted in Fig. 6. The maximum of axial velocity fluctuation is given in Fig. 6(a), and its radial location is given in Fig. 6(b). Initially, the fluctuation levels are negligible. Then, the step induces a strong increase due to the recirculating flow, followed by a quick fall in the throat area. A similar trend can be qualitatively observed on the vorticity fields in Fig. 4. The vorticity intensity greatly increases downstream of the step [Fig. 4(b)]. Then, the flow acceleration in the nozzle induces relaminarization, tends to thin the boundary layer, and decreases the vorticity intensity. It explains the fluctuation drop at the throat. This is corroborated by the maximum location which moves

closer to the wall at the throat. Despite relaminarization, large vortical structures are still noticeable at the throat [Fig. 4(c)]. Significant vorticity [Fig. 4(d)] and fluctuation levels ($\geq 2\%$) are saved downstream in the divergent up to the nozzle exit [Fig. 4(e)] which should lead to a proper early shear layer destabilization. The additional fluctuation raise before the nozzle exit is attributed to a small flow separation occurring at the lips. Such a separation is not expected to occur for the present jet parameters (see Sec. II A 1) according to Morrisette and Goldberg's criterion,[55] i.e., $p_j/p_\infty < 0.3$ at M = 3.1. However, a separation has also been obtained in the simulation by Liu *et al.*[53] where the criterion, i.e., $p_j/p_\infty < 0.65$ at M = 1.5, is not met either. It can be explained as a side effect of the wall mesh refinement which allows us to capture the subsonic sub-boundary layer and favor the flow separation in the case of overexpanded exit conditions. The separation goes up to $0.17D$ upstream of the nozzle exit and is about $0.015D$ wide, as illustrated in Fig. 7(a), which implies to consider that D_j is only equal to 97% of the actual nozzle exit diameter D. This correction is systematically applied (superscript $*$), except for domain dimensions. The separation is strictly steady and the raise of u'_x for
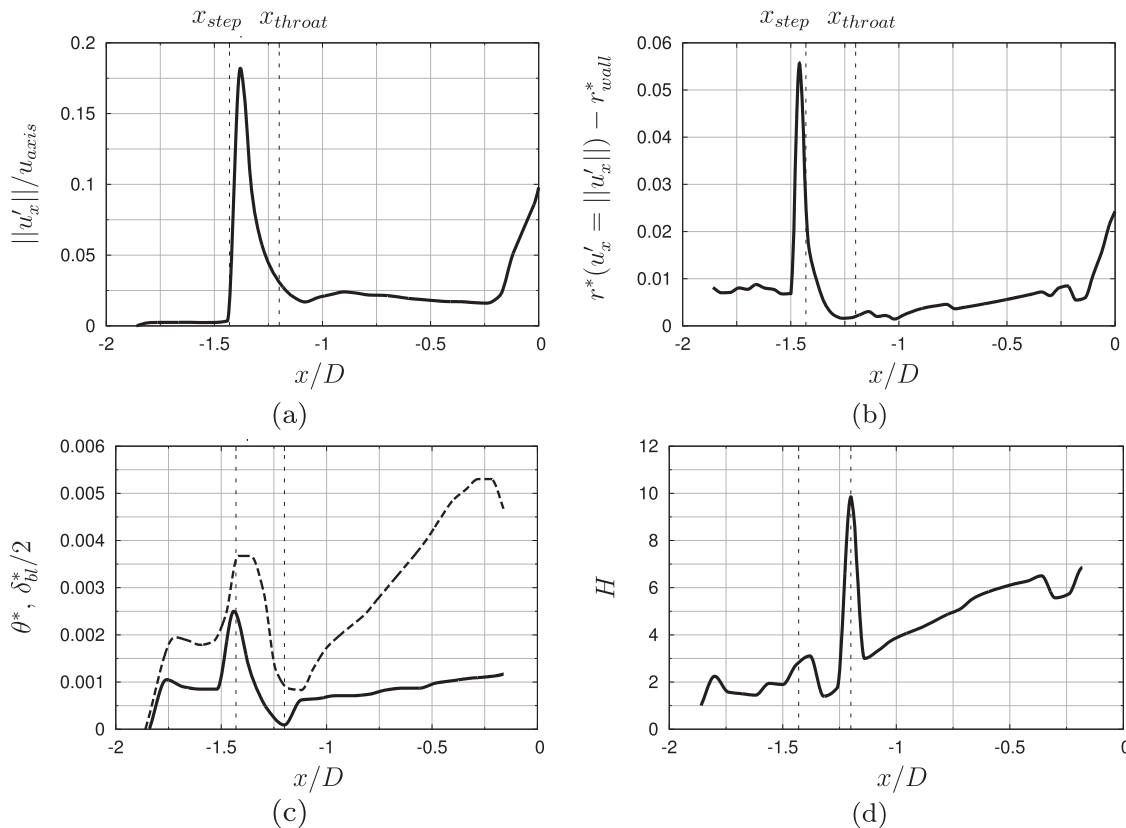
FIG. 6. Nozzle wall boundary layer properties. (a) Maximum of fluctuating velocity, (b) radial location of the maximum of fluctuating velocity, (c) black solid line: momentum thickness $\theta*$ and black dashed line: boundary layer thickness δ^*_{bl}, and (d) shape factor H. The quantities $\theta*$, δ^*_{bl}, and H are not defined in the separated flow region, i.e., $x > -0.17D$.
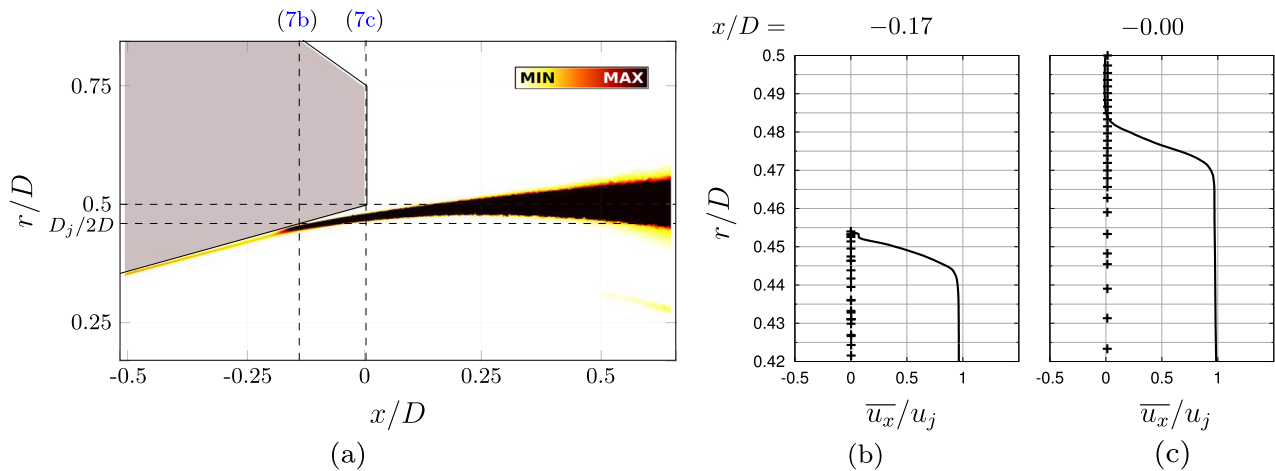
FIG. 7. Mean flow in the vicinity of the separation point. (a) Visualization of the u_x RMS field, (b) $\overline{u_x}$ radial profile at $x = -0.17D$ (separation point), and (c) $\overline{u_x}$ radial profile at $x = -0D$ (nozzle exit). Black solid line: numerical data and black pluses: unstructured mesh discretization every 2 points.

$x > -0.17D$ can be more likely attributed to a standard free shear layer behavior since the flow is not guided anymore by the nozzle wall in this region. Given the local pressure inside the jet, the ambient air is sucked in, inducing a counter flow as noticeable on the profile in Fig. 7(c).

The boundary layer dimensionless thickness δ_{bl}^*, displacement thickness δ_*, momentum thickness θ_*, and shape factor H are given in Fig. 6. This quantities are calculated for the present compressible flow according to

$$\delta_{bl}^*(x^*) = \left[r_{wall}^*(x^*) \mid u(x^*, r^*) = 0.0 \right] \\ - \left[r^*(x^*) \mid u(x^*, r^*) = 0.99 \parallel u(x^*, r^*) \parallel \right], \quad (3)$$

$$\delta^*(x^*) = \int_{r_{wall}^*}^{0} \left(1 - \frac{\rho(x^*, r^*) u(x^*, r^*)}{\rho_0 u_0} \right) dr^*, \quad (4)$$

$$\theta^*(x^*) = \int_{r_{wall}^*}^{0} \frac{\rho(x^*, r^*) u(x^*, r^*)}{\rho_0 u_0} \left(1 - \frac{u(x^*, r^*)}{u_0} \right) dr^*, \quad (5)$$

$$H(x^*) = \frac{\delta^*(x^*)}{\theta^*(x^*)} \quad (6)$$

with the approximation of a negligible wall curvature in the azimuthal direction, i.e., $\delta_{bl}^* \ll r_{wall}^*$. The momentum thickness variations close to the step and the nozzle exit are not relevant since the boundary layer is detached at these locations. In the neighborhood of the throat, it gets smaller due to the boundary layer thinning. Downstream in the divergent, the metrics δ_{bl}^* and θ_* grow linearly which indicates that the boundary layer is developing. A number of grid points across the boundary layer from 5 at the throat to 15 at the separation point are estimated in this region. The shape factor H takes

high values induced by the supersonic convergent-divergent configuration. Indeed, for a standard Blasius boundary layer profile, $H = 2.59$ is considered laminar, while $H \leq 1.4$ is typically turbulent.[56] For fully turbulent boundary layers in high-speed compressible flows, the typical shape factor has been found to increase with the Mach number. For instance, Maeder et al.[57] have carried out a Direct Numerical Simulation (DNS) of a boundary layer on a flat plate at three mean flow Mach numbers from $M_\infty = 3$ to 6 and obtained turbulent shape factors from $H = 5.86$ to 17.20. In the present situation, H therefore gradually increases downstream of the throat because of the flow acceleration. A value of $H \simeq 7$ is obtained at the nozzle exit, where $M_j = 3.1$, which is probably not a fully turbulent condition. However, the geometrical tripping does not aim at providing such an exit condition but only sufficient velocity fluctuations to ensure the early shear layer destabilization at the lips. As shown by Fig. 6(a), this requirement is met in practice despite the relaminarization phenomenon.

III. SIMULATION VALIDATION

The full free jet computation is validated in this part, with focuses on the aerodynamic in Sec. III A and the acoustic in Sec. III B. The data from the present simulation are compared to available measurements from the MARTEL facility, previous computations, data from the literature, semi-empirical models, and analytical laws in order to estimate its accuracy and predictivity.

A. Aerodynamic

#### 1. Snapshots and mean field visualization

Mean flow fields and snapshots are presented in Figs. 8 and 9 for a qualitative description of the jet near field. Main numerical recording points and profiles are depicted in
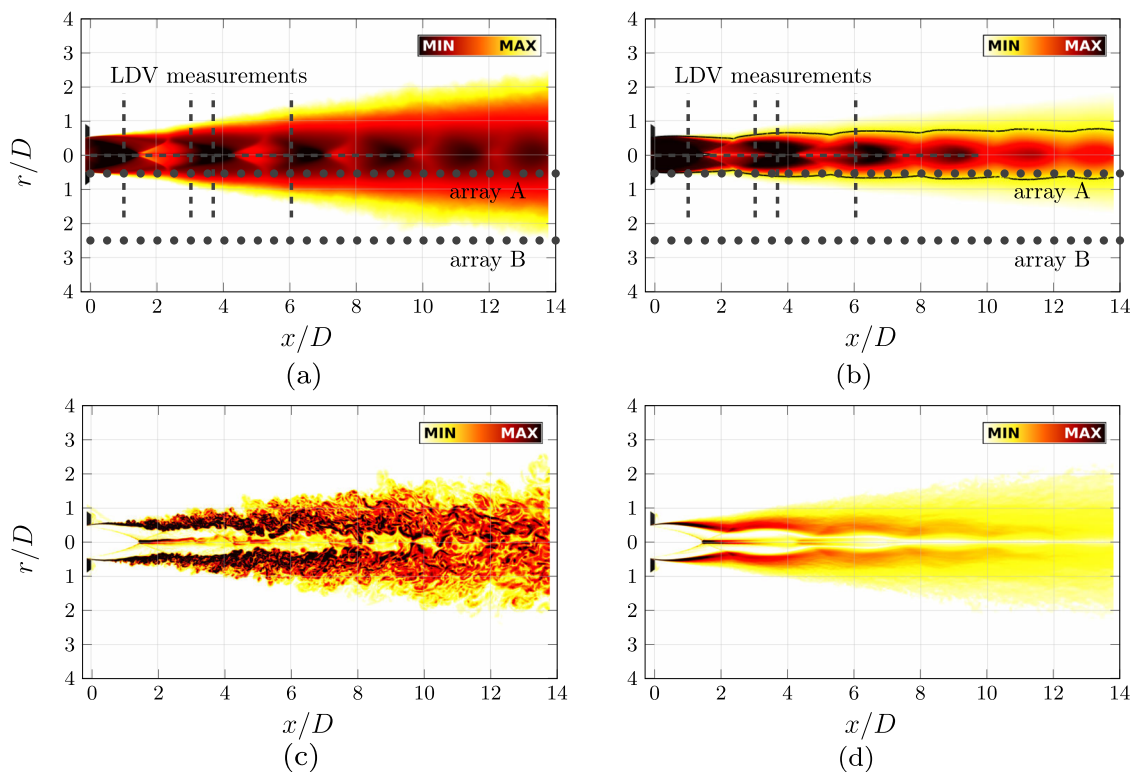
FIG. 8. Visualizations of the (a) mean density field, (b) mean Mach number field, (c) instantaneous vorticity field, and (d) mean vorticity field. Grey circle: numerical arrays; grey dashed line: LDV measurement locations; black solid line: sonic line $M = 1$.

Figs. 8(a) and 8(b). The dashed lines correspond to LDV measurements, while the symbols (grey circles) represent cylindrical numerical arrays at $r = 0.5D$ (lipline) denoted as array A and $r = 2.5D$ denoted as array B. The mean density field is displayed in Fig. 8(a) in colored levels. The ejected combustion gas has a lower density than the ambient air because of the high temperature and the overexpanded condition. The species mixing layer seems to spread linearly. Compressible effects are noticeable through the shock cell structure, as well as on the Mach number field in Fig. 8(b). The drawn sonic

line illustrates that the flow in the shear layer is strongly deviated by the successive expansion fans and compressions of the shock cell structure. Array A is essentially located in a supersonic zone. Instantaneous and mean vorticity fields are given in Figs. 8(c) and 8(d), respectively. They show that the shear layer is destabilizing early and spreading properly which is a major improvement compared to the previous computation.[44] Downstream, a wide variety of vortical structure sizes can be seen on the transversal snapshots in Figs. 8(c) and 9, which suggests a proper shear layer development. The shear
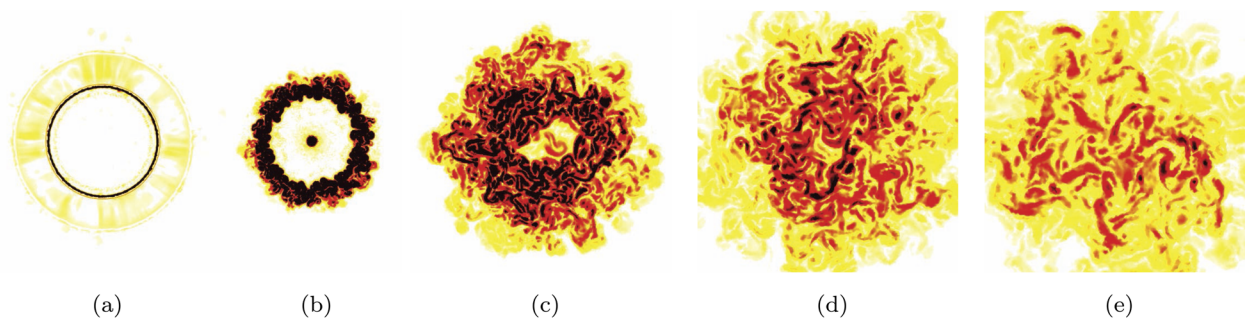
FIG. 9. Dimensionless transversal cut of vorticity in the free jet region at various axial locations. (a) $x = 0.0D$, (b) $x = 1.33D$, (c) $x = 5.0D$, (d) $x = 10.0D$, and (e) $x = 15.0D$.

layer periodic deviation due to the shock cells is particularly visible on the mean vorticity field. Triple-points delimiting a small Mach disk are captured at the initial shock convergence point inside the potential core, at $x = 1.33D$ [Fig. 9(b)], and appear to generate significant vorticity levels. Such an effect can also be observed in the simulation of Liu et al.[53] In order to make further discussions clearer, the visualized jet structure is sketched in Fig. 10. It points out that the shocks are not identically axially located on the centerline and on the lipline.

2. Centerline properties

The mean velocity, the velocity fluctuation magnitude, the Mach number, and the axial velocity skewness and kurtosis along the jet centerline are plotted in Fig. 11. The present results are confronted to the experimental measurements and numerical data from previous computations.[44] The mean velocity in Fig. 11(a) agrees with the experiment in terms of shock locations. The numerical profile shows, however, a strong undershoot at the first shock, also present at a lesser extent in data from Langenais 2017.[44] On the other hand, a large difference of turbulence intensity between the computation (<0.5%) and the experiment (>6%) is highlighted upstream of the first shock in Fig. 11(b). The implemented geometrical tripping method (see Sec. II D) does not enable us to provide fluctuations on the centerline, while the actual nozzle input conditions in the experiment result from a turbulent combustion not included in the simulation. This could explain the discrepancies of turbulence levels on the axis before the first shock. Velocity fluctuations on the jet centerline inducing shock oscillations could also explain the smoother mean velocity profiles in the experiment, in addition to possible LDV measurement bias such as particle polydispersity, coalescence, and lag.[58] The turbulence level downstream of the first shock is much higher and agrees with the experiment for $1.33 < x_* < 10$. Then it slowly decreases downstream of the end of the

potential core, as expected for a fully turbulent jet. The disturbances generated by the triple-points lead to a major improvement compared to previous computations where the simulated levels really started to increase only further downstream for $x_* > 5$.

Based on Figs. 11(a) and 11(c), the dimensionless length of the first shock cell on the centerline is estimated as $L_{1st\,shock}^* = 2.6$ for both the experiment and the simulation. It can be approximated with Tam and Tanna's model[59] derived from the instability wave theory

$$L_{1st\,shock}^* = K\pi\left(M_d^2 - 1\right)^{0.5}\frac{D_d}{\mu_1 D_j},\tag{7}$$

where $M_d = 2.8$ is the equivalent ideally expanded jet Mach number at the exit diameter $D_d = 51$ mm, $\mu_1 = 2.405$ and K is a correction constant. Initially set to $K = 1$, Tam et al.[60] recently recommended to take $K = 0.9$ which yields $L_{1st\,shock}^* = 2.6$ and matches with the simulation. The dimensionless supersonic region mean length can be estimated with the Mach number profile on the centerline, leading to $L_{sonic}^* \simeq 21$. It is slightly longer than in the previous computations.

The skewness S and kurtosis K are defined for a discrete signal s by

$$S(s) = \frac{\overline{s^3}}{\sigma^3} = \frac{\frac{1}{N}\sum_i(s_i - \overline{s})^3}{\left[\sqrt{\frac{1}{N}\sum_i(s_i - \overline{s})^2}\right]^3}\tag{8}$$

and

$$K(s) = \frac{\overline{s^4}}{\sigma^4} = \frac{\frac{1}{N}\sum_i(s_i - \overline{s})^4}{\left[\sqrt{\frac{1}{N}\sum_i(s_i - \overline{s})^2}\right]^4},\tag{9}$$

where $\overline{s^3}$ and $\overline{s^4}$ are the third and fourth statistical moments, respectively, $\overline{s}$ is the mean, σ is the standard deviation, and N is the number of samples of the signal. These metrics measure the asymmetry and the tailedness of the signal probability
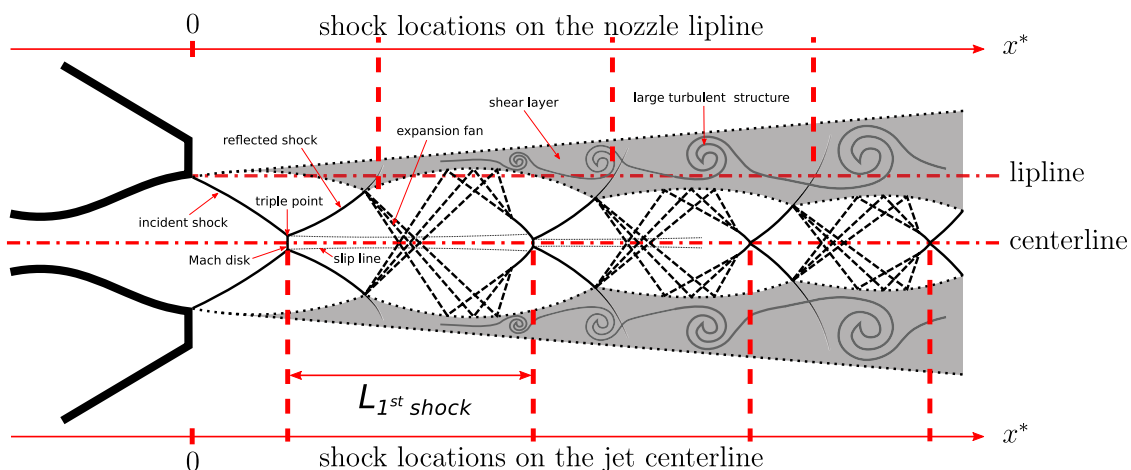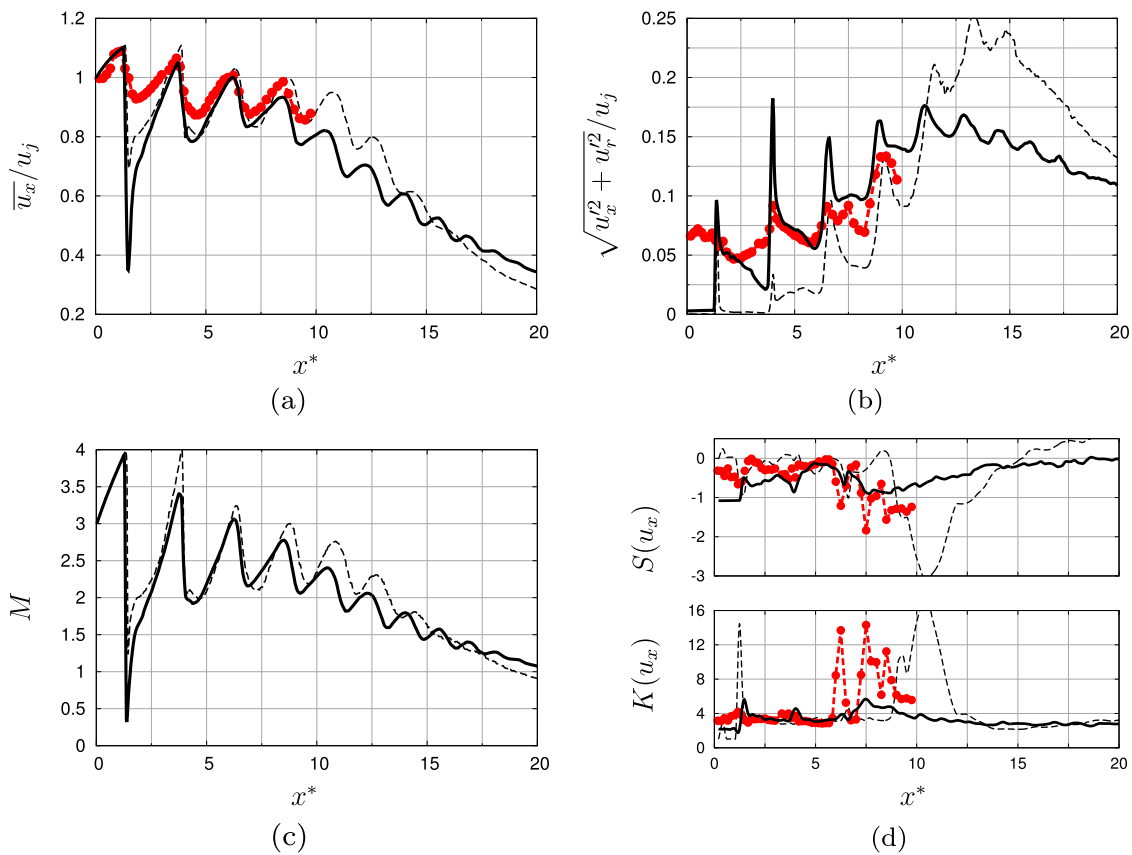

FIG. 10. Sketch of the overexpanded jet structure based on the field visualizations in Fig. 8.

FIG. 11. Velocity properties along the jet centerline. (a) Mean axial velocity, (b) fluctuating velocity, (c) axial Mach number $\overline{u_x}(x^*)/\overline{c}(x^*)$, where $\overline{c}(x^*)$ is the local mean speed of sound, and (d) axial velocity skewness and kurtosis. Red dotted-dashed line: experimental data; black solid line: present numerical data; black dashed line: numerical data from Langenais 2017.[44]

distribution and are equal to $S(s) = 0$ and $K(s) = 3$ in the case of a Gaussian distribution. The skewness and kurtosis of the axial velocity along the centerline are plotted in Fig. 11(d). The main experimental trends are better recovered than in the previous computation at the right locations. The negative peaks of S and positive peaks of K at $x* = 6.2$ and $x* = 7.5$ are captured. Levels are, however, not in accordance with the LDV measurements, especially K. It could be explained by the fact that these metrics are sensitive to the signal length and the sampling rate[43] and that the turbulence properties are not similar on the jet axis in the simulation and the experiment as mentioned above.

3. Shear layer development

Experimental data from the MARTEL facility include radial profiles of mean and fluctuating velocity at the four axial locations $x* = 1, 3, 3.67$, and 6. They are compared to the previous and the present simulation results in Fig. 12. The mean profiles of axial [Fig. 12(a)] and radial [Fig. 12(c)] velocity from the present simulation exhibit a significant improvement compared to the previous simulation. The turbulence tripping

results in a major benefit in terms of velocity fluctuation levels and shear layer development, as reported in Figs. 12(b) and 12(d). The numerical profiles of fluctuating radial velocity show the larger deviation from measurements, while levels are globally recovered. The agreement is particularly satisfactory for the fluctuating axial velocity.

The half velocity jet radius $\delta_{0.5}^*$, the shear layer thickness δ_{sl}^*, and the incompressible shear layer momentum thickness θ_{sl}^* can be calculated from the velocity profiles according to

$$\delta_{0.5}^*(x^*) = r(x^*) \mid u(x^*, r^*) = 0.5u(x^*, 0), \tag{10}$$

$$\delta_{sl}^*(x^*) = [r(x^*) \mid u(x^*, r^*) = 0.05u(x^*, r_0(x^*))] \\ - [r(x^*) \mid u(x^*, r^*) = 0.95u(x^*, r_0(x^*))], \tag{11}$$

$$\theta_{sl}^*(x^*) = \int_{r_0(x^*)}^{\infty} \frac{u(r^*, x^*)}{u_0}\left(1 - \frac{u(r^*, x^*)}{u_0}\right)dr^*, \tag{12}$$

where the lower bound $r_0(x*)$ is arbitrarily set to make the integrated values free from the shock cell presence. The
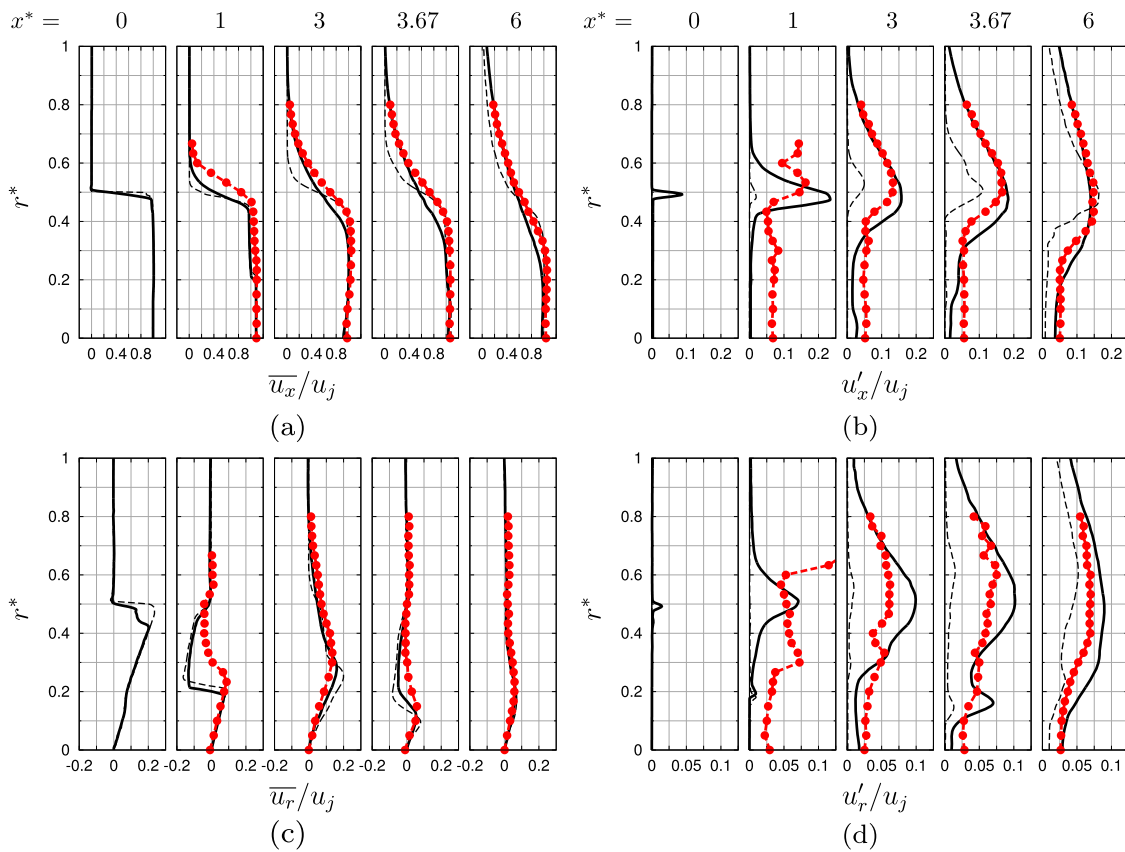
FIG. 12. Radial profiles of mean (a) axial and (c) radial velocity, and fluctuating (b) axial and (d) radial velocity. Red dotted-dashed line: experimental data; black solid line: present numerical data; black dashed line: numerical data from Langenais 2017.[44]

incompressible approximation is *a priori* not suited for this flow. However, the density measurements are not available in the experimental database. The thicknesses are consequently calculated assuming $\rho(x_*, r_*) = \rho_0$ for comparison purposes. These quantities, as well as the magnitude of u'_x/u_j, are plotted along the lipline (array A) in Fig. 13. The simulation is found to agree with the experimental data. The fluctuation levels along array A in Fig. 13(b) are similar, for example $u'_x/u_j \simeq 0.15$ at $x_* = 1$. The nearly null initial value is due to the fact that the closest recording points to the lips on array A are located outside the shear layer knowing that the flow is separated. The numerical asymptotic spread rate of the shear layer is $d\delta^*_{sl}/dx = 0.13$ as shown in Fig. 13(c) which is close to the estimated experimental value 0.11. In the same way, the asymptotic spread rate of the momentum is found to be $d\theta^*_{sl}/dx = 0.022$ numerically and 0.020 experimentally. These values are consistent with the experimental results of Troutt and McLaughlin[61] studying a $M_j = 2.1$, $Re_D \sim 10^6$ jet, reported in Fig. 13(c), or Hussain and Zedan[26] studying initially disturbed laminar shear layers. The latter have found spread rates of $d\delta^*_{sl}/dx = 0.16$ and $d\theta^*_{sl}/dx = 0.029$ for a shear layer with an initial velocity fluctuation intensity $u'/u_j = 0.08$ and have shown

that these values decrease by increasing Re_D or decreasing u'/u_j. They have also concluded that the self-preserving zone, i.e., with a linear spread rate, is quickly reached downstream of the separation point as obtained in the present simulation.

The dimensionless potential core length L^*_{core} is estimated considering the half velocity jet width $\delta^*_{0.5}$ in Fig. 13(a) and the shear layer width δ^*_{sl} in Fig. 13(c). This length is defined as the axial location for which $\delta^*_{sl} = 2\delta^*_{0.5}$ leading to $L^*_{core} \simeq 8$ and is reported in Fig. 13. It is found shorter than in the previous computation. This value also appears to deviate with most of the empirical models known in the literature such as the formulas of Nagamatsu and Horvay, Eldred, or Lau. Many authors found that the potential core shortens while increasing the jet temperature. According to Greska et al.,[62] these models are not validated for hot supersonic jets and cannot readily take into account the temperature effect via the only dependence on the Mach number. Greska et al.[62] consequently proposed a new formulation for hot jets with an exponential correction term

$$L^*_{core} = 3.134 \exp\left(1.043M_d - M_c\right) \times \frac{D_d}{D_j} = 8.6, \tag{13}$$
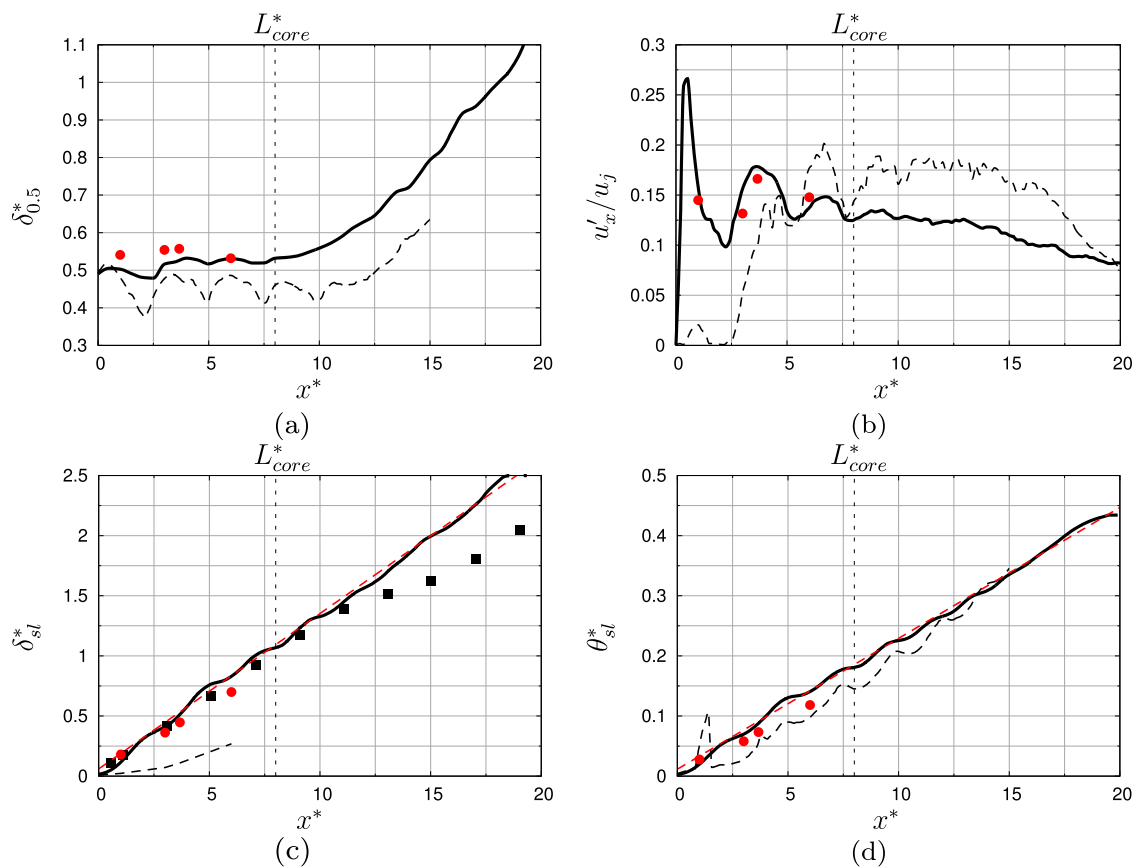
FIG. 13. Free jet shear layer properties. (a) Half velocity thickness, (b) fluctuating axial velocity along the lipline (array A), (c) shear layer thickness, and (d) momentum thickness. Red circles: experimental data from MARTEL; black squares: experimental data from Troutt and McLaughlin[61] (M_j = 2.1, $Re \sim 10^6$); black solid line: present numerical data; black dashed line: numerical data from Langenais 2017;[44] red dashed line: asymptotic spread rates $d\delta_{sl}^*/dx^* = 0.13$ and $d\theta_{sl}^*/dx^* = 0.022$.

where M_c is the convective Mach number defined by $M_c = u_j/(c_j + c_\infty) = 1.9$. This model is in better agreement with the simulation. However, the faster decrease of the centerline velocity in Fig. 11(a) and the small overestimation of the shear layer spread rate in Fig. 13(c) regarding the experimental data suggest that L_{core}^* could be still underestimated in the simulation.

The shear layer shows realistic features, and the turbulent structures seem to properly develop in Figs. 8(c) and 9. Azimuthally averaged PSDs of the axial velocity are plotted for different x_* along array A in Fig. 14 in order to quantitatively check that the turbulence has correct physical properties. Broadband spectra can be seen in Fig. 14(a) without significant peaky values. The levels quickly drop at frequencies $St \geq 0.1$ according to a $St^{-5/3}$ slope for all spectra which indicates a proper turbulent energy cascade. The cut-off frequency of the flow solution is reduced when moving downstream due to the mesh coarsening but remains higher than the expected value $St_c = 0.3$ in the acoustic near field (see Sec. II C 2). The velocity spectra at all axial locations on array A

are presented as a spectrogram function of x_* in Fig. 14(b). The shock cells have an important effect on the fluctuation spectra. The intensity rises and reaches a maximum just downstream of the shock before falling till the next shock. This phenomenon is particularly noticeable for the first two shock cells at high frequencies. It can be associated with both the shock/turbulence interaction amplification effect[63] and the shear layer deviation pointed out in Sec. III A 1 [see Fig. 8(d)]. The spectrogram also highlights that mid frequency fluctuations are dominant for $x^* < L_{core}^*$, while low frequency fluctuations associated with large turbulent structures are prevalent downstream.
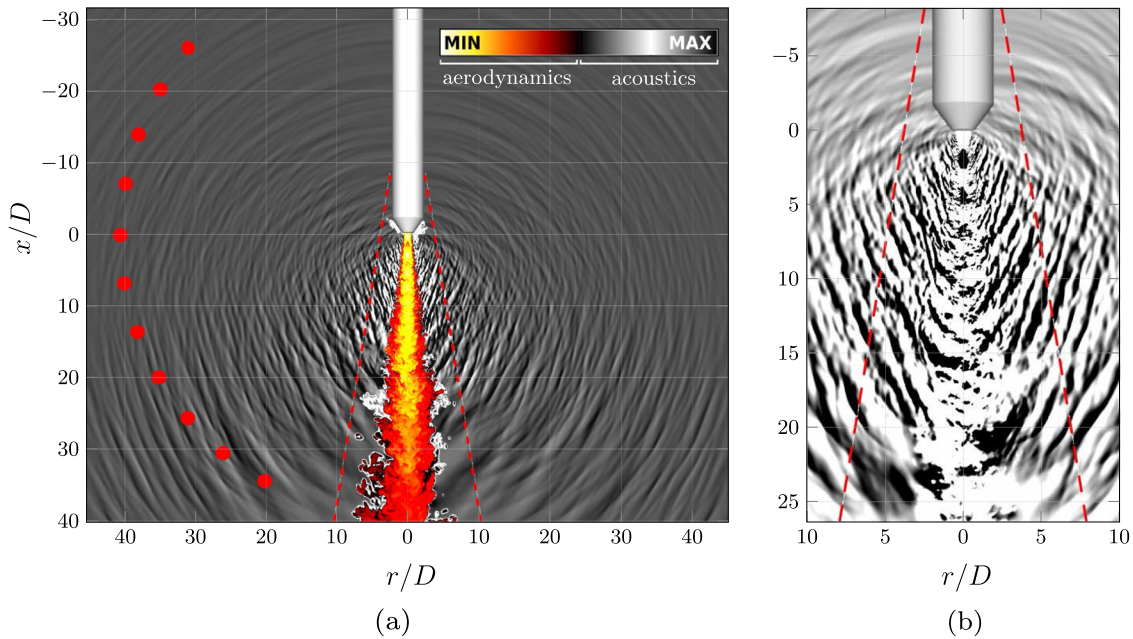
B. Acoustic

1. Snapshot visualization

The agreement of the flow solution with the experimental measurements and other available data suggests that the noise generation is properly predicted. Snapshots of the density and pressure fields in Fig. 15 do not show any discontinuity
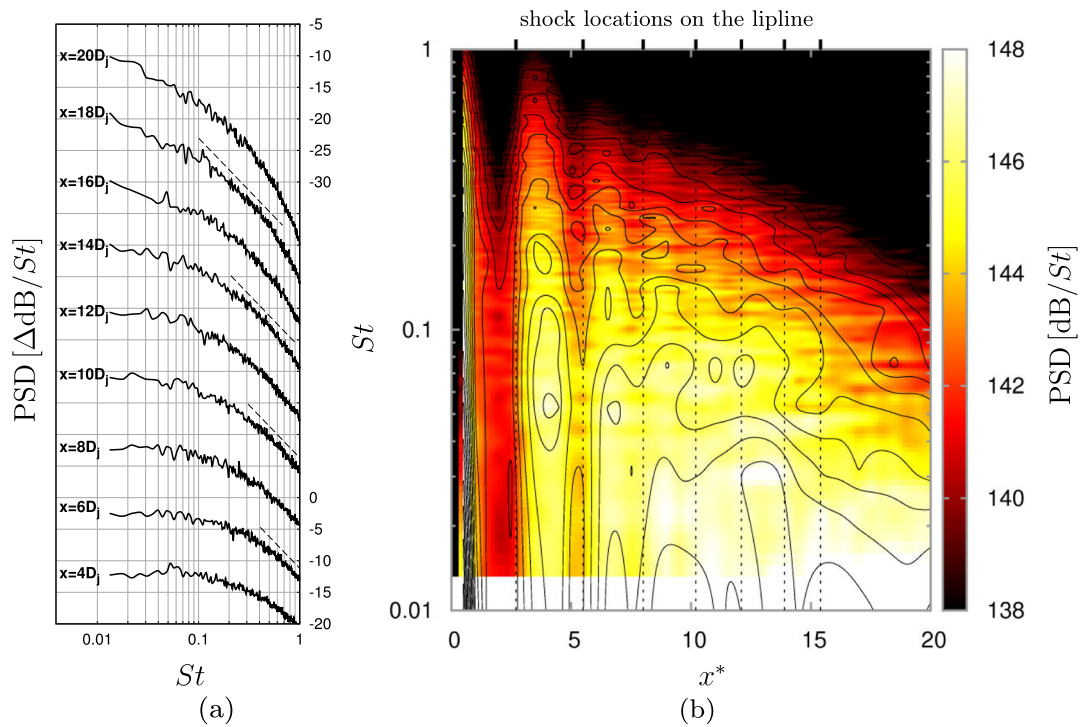
FIG. 14. PSDs of the axial velocity measured in the shear layer along the lipline (array A) with (a) PSDs offset by 10 dB from others and (b) spectrogram function of $x*$. Black solid line: present numerical data; black dashed line: $St^{-5/3}$ slope (Kolmogorov law); black line: PSD iso-lines every $\Delta 1$ dB/St.

FIG. 15. Visualization of the (a) density near and far field and (b) pressure near field. Red dashed line: coupling interface and red circles: far field microphone locations.
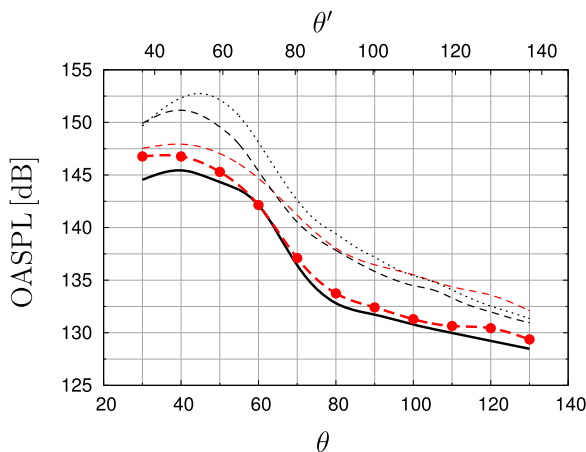
at the coupling interface. The acoustic waves seem to be propagated without significant numerical damping. The expected peak directivity associated with the Mach wave radiation for such a supersonic jet (see Sec. IV A 1) is recovered downstream. No strong vortical structures are found to cross the interface which should avoid any spurious noise generation concern.
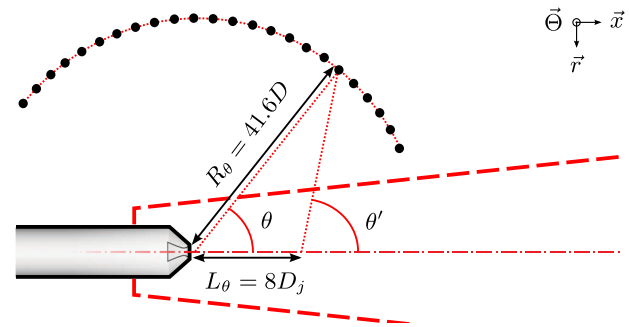
2. Overall levels

The far field acoustic levels computed by the Euler solver at the microphone locations are given in Fig. 16 as a function of the observation angle. The initial angle denoted as θ is centered on the nozzle exit, as illustrated in Fig. 17. As proposed in other studies on supersonic jet noise,[7,64,65] an alternative observation angle θ', centered on the end of the potential core, is defined according to the transformation

$$\theta' = \begin{cases} \arctan\left(\dfrac{\sin(\theta)}{\cos(\theta) - \frac{L_\theta}{R_\theta}}\right) & | \quad \theta < \arccos\left(\frac{L_\theta}{R_\theta}\right) \\ \arctan\left(\dfrac{\sin(\theta)}{\cos(\theta) - \frac{L_\theta}{R_\theta}}\right) + \pi & | \quad \theta > \arccos\left(\frac{L_\theta}{R_\theta}\right) \end{cases}, \quad (14)$$

where $L_\theta = L_{core} = 8 \pm 1D_j$ and $R_\theta = 41.6D$. Considering an uncertainty of $1D_j$ for L_{core}, the uncertainty propagated to θ' is about $1°$. The transformation is illustrated in Fig. 17 and reported on the top axis in Fig. 16. The overall sound pressure levels (OASPL) are calculated from the pressure signals by integrating the PSDs over a finite frequency range. The experimental and numerical PSDs are integrated over the same range for a fair comparison. The lower bound is set to $St = 0.01 > St_{min}$ which is slightly higher than the MARTEL facility absorption device cutoff estimated as $St = 0.007$

FIG. 17. Observation angle transformation from θ to θ' centered on the end of the potential core.

($\simeq 200$ Hz). The upper bound is set to the simulation cutoff $St_c = 0.22$.

Considering this frequency bandwidth, the simulation finely agrees with the measurements. It is a major improvement compared to the previous Navier-Stokes-Ffowcs Williams and Hawkings computation, as depicted in Fig. 16. The specific influence of the method (FWH vs Euler) on this result is discussed later in Sec. IV D 3. The slightly higher experimental levels at shallow angles could be due to a numerical underestimation induced by the mesh coarsening in the zone Z1 for $x_* > 20$ (see Sec. II C 2), or spurious ground reflections in the experiment despite the wedges. Nevertheless, the directivity shape is captured. The numerical peak directivity is located at $\theta_{peak} \simeq 40°$ which corresponds to $\theta'_{peak} \simeq 48°$.

3. Power spectral densities

The numerical PSDs at the four angles $\theta = 30°$, $60°$, $90°$, and $120°$ are compared to those from the experimental acoustic signals in Fig. 18. The PSDs are calculated using the Welch method with a 50% block overlapping and a natural windowing as recommended for broadband spectra. Experimental and numerical signals are averaged over 1000 and 11 blocks, respectively, resulting in frequency resolutions $\Delta St = 0.005$ and 0.01. The high level broadband spectra at shallow angles are characteristic of Mach wave radiation. The peaks in medium frequencies at larger angles are due to the additional broadband shock-associated noise (see Sec. IV A 2) which becomes dominant in the side and upstream directions and induces a bump on spectra [see Fig. 18(d)]. The agreement between the simulation and the experimental data is satisfactory over the resolved frequency bandwidth which indicates that the main features of the acoustic field are properly predicted. The effective cut-off frequency is found to be equal to the expected value $St_c = 0.22$. The mid frequency levels are finely reproduced for $\theta \geq 60°$, including the shock-associated bump. Low frequencies are slightly underestimated in the upstream direction, as high frequencies at $\theta = 30°$, explaining the previously mentioned level deficit at smallest angles in Fig. 16. Differences are

FIG. 16. OASPL at the far field microphone location functions of θ and θ'. Experimental PSDs integrated, red dotted-dashed line: over the range $0.01 \leq St \leq 0.22$ and red dashed line: over the full spectrum; black solid line: present numerical PSDs integrated over the range $0.01 \leq St \leq 0.22$; black dotted line/black dashed line: numerical PSDs from Langenais 2017[44] integrated over the range $0.01 \leq St \leq 0.22$ using the NS-FWH/NS-Euler approach, respectively.
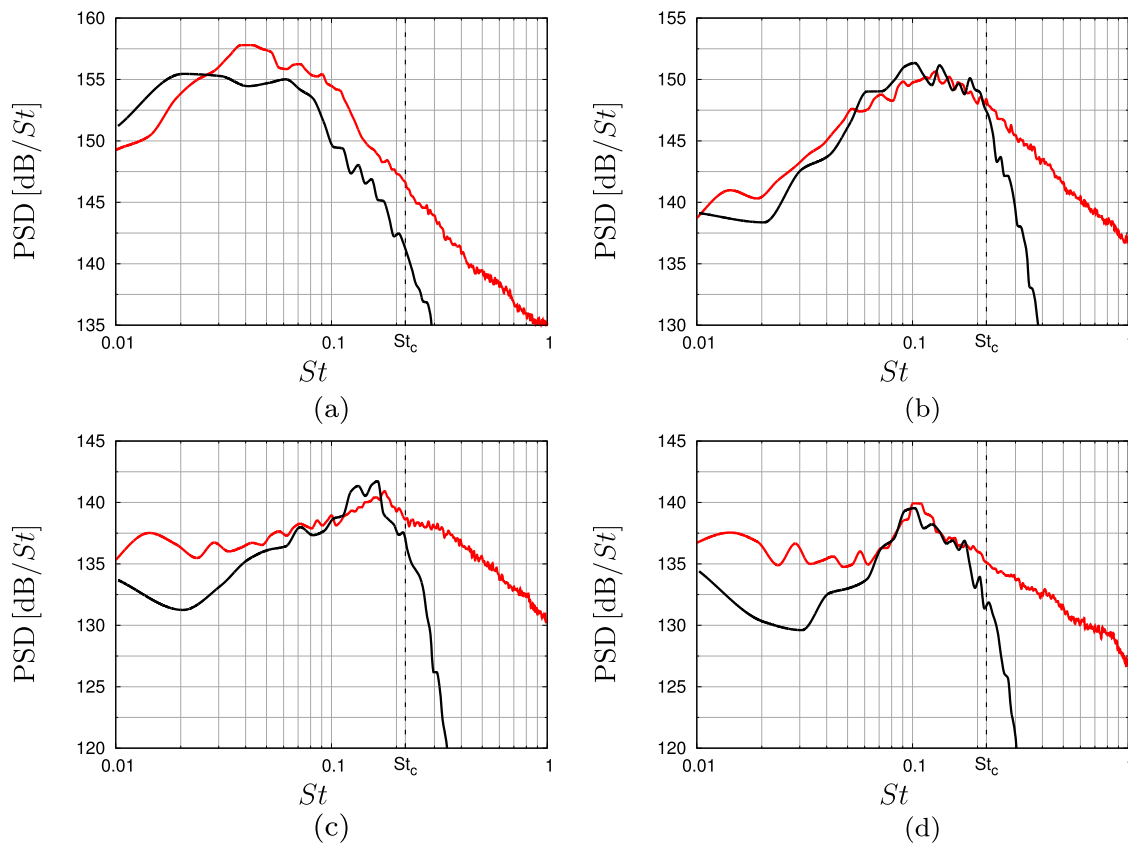
FIG. 18. PSDs of the pressure at four observation angles. (a) $\theta = 30°$ ($\theta' = 36.6°$), (b) $\theta = 60°$ ($\theta' = 70.4°$), (c) $\theta = 90°$ ($\theta' = 100.9°$), and (d) $\theta = 120°$ ($\theta' = 128.6°$). Red solid line: experimental data and black solid line: present numerical data.

also observed at low frequencies $St < 0.02$ which could reveal test bench environmental effects, such as spurious low frequency reflections, or a lack of numerical convergence. Finally, a significant part of the dominant acoustic spectra is not properly simulated at high frequencies with respect to the experimental data due to the limited cut-off frequency.

IV. ANALYSIS OF THE RADIATED NOISE

The agreement of the simulation with most of the available aerodynamic and acoustic data is demonstrated at this point, and the results can therefore be relevantly exploited for physical analysis. The aeroacoustic near and far fields are described and analyzed in this part, with emphasis on the noise sources in Sec. IV A, the resulting pressure near field in Sec. IV B, the pressure far field in Sec. IV C, and the non-linear propagation effects in Sec. IV D. Simple and double Fourier transforms, cross correlations, and azimuthal mode decomposition are applied to characterize the noise properties. Specific metrics are then calculated to identify nonlinear effects.

A. Jet noise sources

The noise from imperfectly expanded supersonic jet is admitted to be generated by three main mechanisms:[2,3] the convection of large turbulent structures in the shear layer, the mixing of fine turbulent scales in the shear layer, and the interaction of turbulent structures with shocks. The first one is associated with the Mach wave radiation and the third one with the broadband shock-associated noise.

1. Mach waves

Strong amplitude Mach waves are expected to be generated when large turbulent structures are convected at supersonic speeds relatively to the ambient medium. This mechanism is often described through the wavy wall analogy as shown by Tam.[2] Three main instability wave families initially observed by Oertel *et al.*[66] are expected to produce Mach waves. Their associated convective Mach numbers are

$$M_{c1} = \frac{u_j - c_j}{c_j + c_\infty} = 1.3, \tag{15}$$

$$M_{c2} = \frac{u_j}{c_j + c_\infty} = 1.9, \tag{16}$$

$$M_{c\,3} = \frac{u_j + c_j}{c_j + c_\infty} = 2.5. \tag{17}$$

Given that the Mach wave appearance conditions $M_{c\,2} > 0.8$ and $M_{c\,3} > 1.25$[62,67] are met and that the convective Mach numbers are all supersonic, the three kinds of instability waves are expected to radiate Mach waves at Mach angles θ'_{M_n} defined by

$$\theta' = \arccos\left(\frac{1}{M_c}\right) \tag{18}$$

yielding $\theta'_{M_{c1}} = 40°$, $\theta'_{M_{c2}} = 58°$, and $\theta'_{M_{c3}} = 66°$. The transformed angle system centered on the end of the potential core as defined by Eq. (14) is used here because it is considered as a better approximation of actual radiation directions. The convection velocities of the turbulent structures with respect to the ambient medium can also be calculated by performing a double fast Fourier transform (FFT) in time and space, noted $\widehat{\widehat{p}}$ for the pressure, or cross correlations inside the jet shear layer. These approaches lead to the results depicted in Fig. 19. The normalized magnitude of the double FFT function of the dimensionless wave number kD_j (transform in space) along array A and St (transform in time) is given in Fig. 19(a). The maximum of the double FFT seems to follow a slope corresponding to a convection speed $u_c/u_j = 0.43$, i.e., $M_c = 2.2$ which is reported as a black dashed line. This value represents the most likely convection speed in the shear layer in the range $0 \le x_* \le 20$ and is close to the slopes deduced from $M_{c\,2}$ and $M_{c\,3}$ reported as gray dashed lines. This result precisely matches with the unique Mach number, referred to as the Oertel convective Mach number, defined by Greska et al.[62] as

$$M_{co} = \frac{u_j + 0.5c_j}{c_j + c_\infty} = 2.2 \tag{19}$$

suggesting that this number could be a key parameter of the Mach wave generation mechanism. The corresponding radiation angle is $\theta'_{M_{co}} = 63°$.

The convection velocity u_c versus x_* in Fig. 19(b) is obtained by cross-correlating the axial velocity recorded at successive probes of array A, spaced by Δx_*, two by two. The convection velocity at a location x_* is deduced from the delay of the maximum correlation, and the results are azimuthally averaged as

$$u_c(x^*) = \int_0^{2\pi} \frac{\Delta x^*}{2\pi\, \tau_{max}(x^*, \Theta)}\, d\Theta \tag{20}$$

given

$$\begin{aligned}[u_x(x^*, t) \star u_x(x^* + \Delta x^*, t)](\tau_{max}) \\ = \max[[u_x(x^*, t) \star u_x(x^* + \Delta x^*, t)](\tau)]. \end{aligned} \tag{21}$$

The initial value is close to 0 due to the previously mentioned flow separation. Three main regions can be deduced from this result. In the early developing shear layer in the range $x_* < 2$, the most coherent structures generated by the mixing are not fully accelerated yet and only the first instability wave family ($M_{c\,1}$) seems to be able to radiate Mach waves. It is probably not correct in practice because array A does not properly follow the shear layer in this region due to its deviation (see Sec. III A 1). Downstream in the range $2 < x_* < 12$, the convection speed reaches its maximum in the vicinity of the 1st shock ($x_* \simeq 3$) and then oscillates around $M_{c\,3}$. Consequently, strong Mach waves are expected to radiate close to the angle $\theta'_{M_{c3}} = 66°$ in this region. The maximum speed at $x_* = 3$ gives the largest possible radiation angle $\theta'_{max} = 70°$. Downstream of the end of the potential core for $x_* > 12$, the convection speed decreases quasi-linearly, especially from M_{co} to $M_{c\,1}$. Mach waves can therefore be generated with various radiation angles roughly in the range $40° < \theta' < 60°$ which is observed in Fig. 15(a).
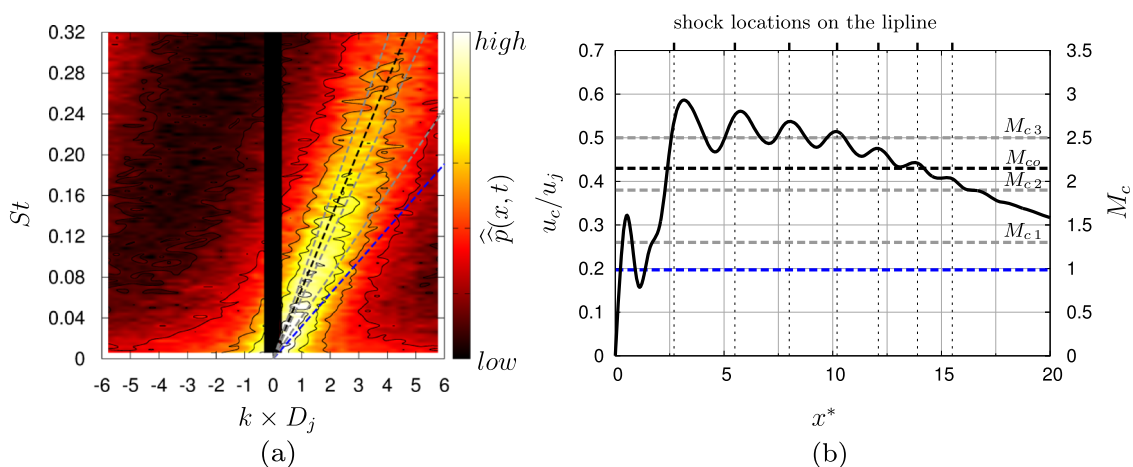
FIG. 19. Estimation of the convection velocity of turbulent structures along the lipline (array A). (a) Normalized double Fourier transform in time and space and (b) convection velocity corresponding to the maximum of the cross correlation of the axial velocity. Black solid line: present numerical data; black dashed line: $u_c/u_j = 0.43$ convection speed; grey dashed line: $M_{c\,n}$ convection speeds [Eqs. (15)–(17)]; blue dashed line: $u_c = +c_\infty$ (supersonic convection threshold).

The analyses from the double FFT and the cross correlations lead to coherent conclusions. The double FFT provides the most likely convection speed and consequently the Mach waves at the most likely radiation angle $\theta'_{M_{co}} = 63°$, while the successive cross correlations indicate that a large variety of Mach waves are possible mainly with radiation angles $\theta'_{M_{c1}} < \theta' < \theta'_{M_{c3}}$. Finally, the Mach waves are often associated with the peak directivity, but θ'_{peak} observed in Fig. 16 cannot be readily linked to $\theta'_{M_{co}}$ because of a further geometrical bias. The Mach wave generation is indeed not localized in a restricted region, and the microphones are not far enough from the sources, especially at shallow angles. Consequently, the observation angle transformation is insufficient to get rid of the geometrical bias at shallow angles.

2. Broadband shock-associated noise

The shock cells are known to produce noise through an interaction mechanism with convected large turbulent structures.[59] This noise source has a broadband spectrum, except when a feedback loop with the early instability wave development occurs, inducing a tonal noise known as screech.[3] The broadband shock-associated noise (BBSAN) is dominant essentially upstream. A model has been proposed by Tam and Tanna[59] to predict the BBSAN peak frequency according to

$$St_{BBSAN} = \frac{u_c}{\overline{L^*_{shock}}(1 - M_c \cos\theta')u_j}, \quad (22)$$

where the dependency on $\cos\theta'$ allows us to take into account the Doppler effect, $\overline{L^*_{shock}}$ is the mean shock spacing, and $M_c = u_c/c_\infty$ is the convective Mach number of the large structures. The mean shock spacing in Tam and Tanna's model is usually approximated via Eq. (7), but for the present jet, the shock spacing is different on the centerline and the lipline and gets significantly shorter when moving downstream. Given that roughly the 2nd to the 5th shocks are known to be the main contributors to the BBSAN, $\overline{L^*_{shock}}$ is consequently estimated as the mean shock spacing between the 1st and the 6th shock in the shear layer, reported in Fig. 19(b), leading to $\overline{L^*_{shock}} = 2.2 \pm 0.6$. The convection Mach number is set equal to $M_{c\,3}$. The formula yields $St_{BBSAN} = 0.15 \pm 0.05$ at $\theta' = 100.9°$ and $St_{BBSAN} = 0.09 \pm 0.02$ at $\theta' = 128.6°$. These values are in agreement with the peak frequencies noticed on the PSDs at the same angles, respectively, in Figs. 18(c) and 18(d). The uncertainties on M_c and $\overline{L^*_{shock}}$ explain the shock-associated noise broadening. When screech noise emerges, its fundamental frequency can be estimated by applying Eq. (22) at $\theta' = 180°$ yielding $St_{BBSAN} = St_{up} = 0.066 \pm 0.018$. Intense discrete peaks at a frequency St_{up} are not observed on the PSDs in the far field, indicating the absence of screech noise as expected for such a hot supersonic jet.[2]

## B. Velocity and pressure near field

1. Spatio-frequency content

Azimuthally averaged PSDs of the pressure signal recorded on array B are plotted as a function of x_* in Fig. 20.

This array is *a priori* located in a purely acoustic region to characterize the near field wave emission. Regarding the shapes in Fig. 20(a), the effective cut-off frequency is larger than the global acoustic cut-off $St_c = 0.22$ which is due to the fact that the cutoff in the zone Z1 is higher (see Sec. II C 2). The spectrogram in Fig. 20(b) shows various behaviors regarding three different regions. For $x_* < 4$, low acoustic levels are found, except for a peak at the frequency $St_{up} = 0.066$ previously highlighted in Sec. IV A 2 as the upstream BBSAN frequency. Since the present jet is not screeching, this peak can simply be attributed to the upstream propagation of the BBSAN. For $4 < x_* < 14$, the spectra are dominated by mid frequencies $St > St_{up}$. For $x_* > 14$ and downstream, the central frequency decreases and reaches higher levels. This decomposition in three regions is reminiscent of the similar analysis presented in Sec. IV A 1. The Mach waves radiating at largest angles in the range $2 < x_* < 12$ on array A can be associated with mid frequencies in the range $4 < x_* < 14$ on array B. The Mach waves radiating at smallest angles in the range $x_* > 12$ on array A can be associated with low frequencies in the range $x_* > 14$ on array B. Moreover, the BBSAN is mostly generated where the shocks are the strongest and turbulent structures sufficiently developed, i.e., roughly $2 < x_* < 16$, at frequencies $St \geq St_{up}$, which is consistent with the spectrogram in the regions $x_* < 4$ and $4 < x_* < 14$.

A double FFT and cross correlations of the pressure signals are performed on array B in the same way as for array A. The resulting normalized magnitude of the double FFT is given in Fig. 21(a). The successive cross correlations provide the dominant wave phase speed along array B and are shown in Fig. 21(b). The phase speed c_φ is not necessarily equal to c_∞ since the waves can propagate in various directions. Assuming the waves are planar fronts having a phase speed c_∞ in the propagation direction, the radiation angle can be estimated by $\theta'' = \arccos(c_\infty/c_\varphi)$. Three different behaviors are once again visible and linked to the previously mentioned three jet regions. For $x_* < 2$, a negative phase speed is found which indicates upstream propagating waves as concluded before. This is corroborated by the double FFT where significant levels are reached, especially at the frequencies $St \geq St_{up}$, along a slope equivalent to a phase speed $c_\varphi/c_\infty = -1.2$ on the negative wave number side. It means that the waves propagate backward regarding array B at an estimated angle $\theta''_{up} = 145°$. Downstream, the phase speed is positive. The peak at $x_* = 3$ could be attributed to the waves emitted in the vicinity of the 2nd shock, associated with early radiating Mach waves and BBSAN. For $4 < x_* < 14$, the phase speed is rather constant around $c_\varphi/c_\infty = 3.3$ where strong directional Mach waves, generated in the region $2 < x_* < 12$ in the shear layer as mentioned in Sec. IV A 1, are propagating. Downstream for $x_* > 14$, the phase speed gradually decreases which is associated with Mach waves radiating at smaller and smaller angles. The maximum levels of the double FFT are found for a wide range of frequencies along the slope corresponding to $c_\varphi/c_\infty = 3.3$. The estimated radiation angle is $\theta'' = 72°$ which is rather consistent with the larger Mach wave radiation angle
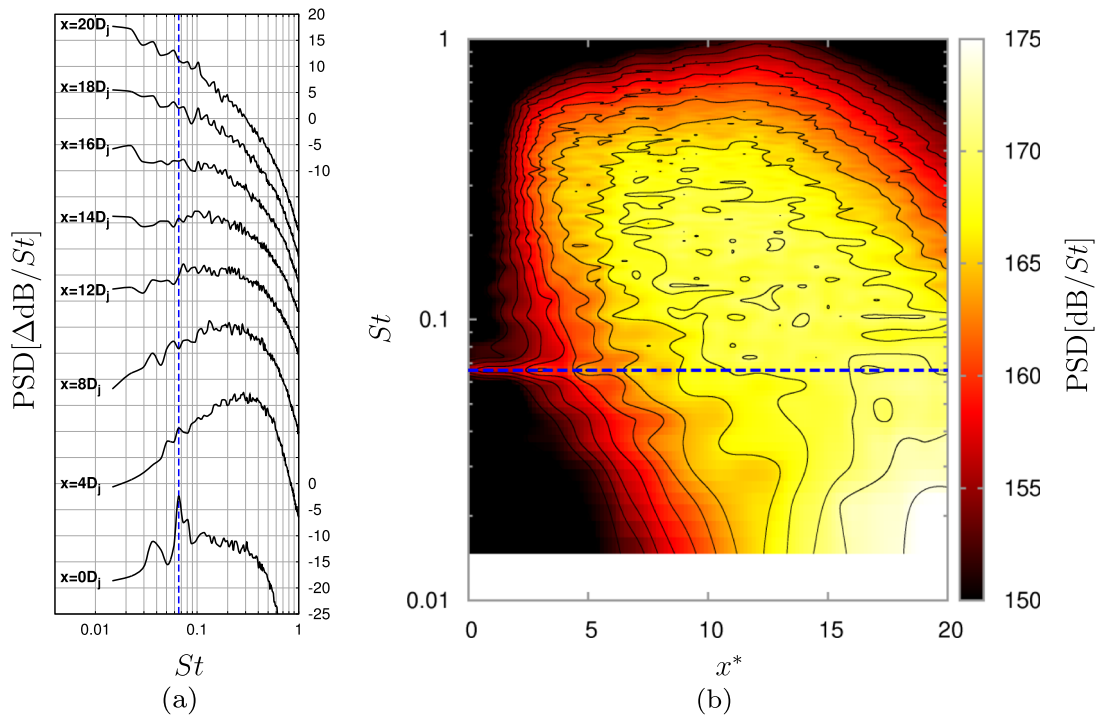
FIG. 20. PSDs of the pressure measured along array B. (a) PSDs offset by 10 dB from others and (b) spectrogram function of $x*$. Black solid line: present numerical data; blue dashed line: $St = St_{up}$; black line: PSD iso-lines every $\Delta 2$ dB/St.

$\theta'_{\max} = 70°$ discussed in Sec. IV A 1. The faint slope corresponding to $c_\varphi/c_\infty = 0.2$, also highlighted on the positive wave number side, is due to slow flow events reaching intermittently array B.

2. Azimuthal content

The spatio-frequency properties of the Mach wave radiation and the BBSAN in the near field are well assessed at this point. The azimuthal properties are also a matter of interest
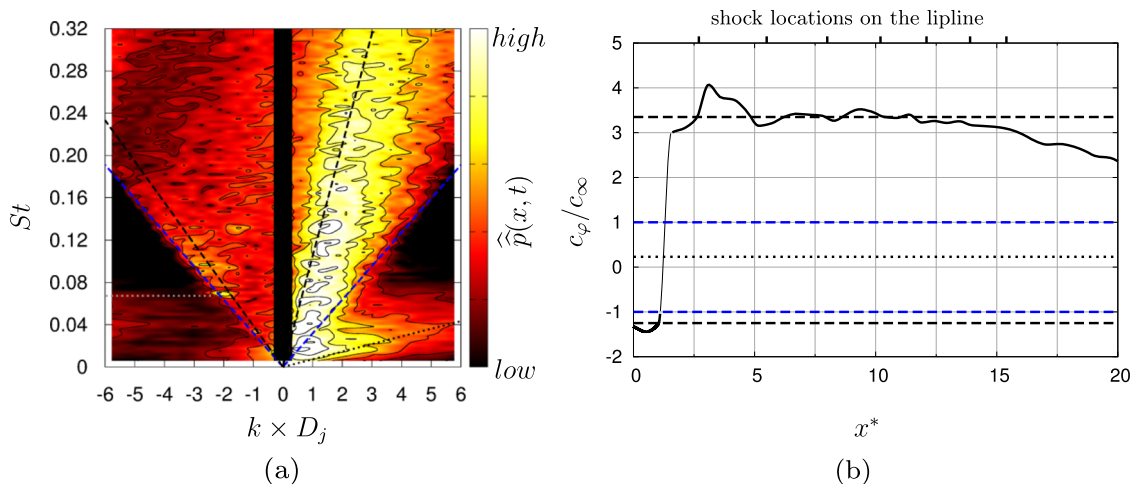
FIG. 21. Characterization of the acoustic wave propagation in the near field. (a) Normalized double Fourier transform in time and space and (b) phase velocity corresponding to the maximum of the cross correlation of the pressure along array B. Black solid line: present numerical data; black dashed line: phase speeds $c_\varphi/c_\infty = -1.2$ backward and $c_\varphi/c_\infty = 3.3$ forward; black dotted line: slow flow component; grey dotted line: $St = St_{up}$; blue dashed line: $c_\varphi = \pm c_\infty$ thresholds.
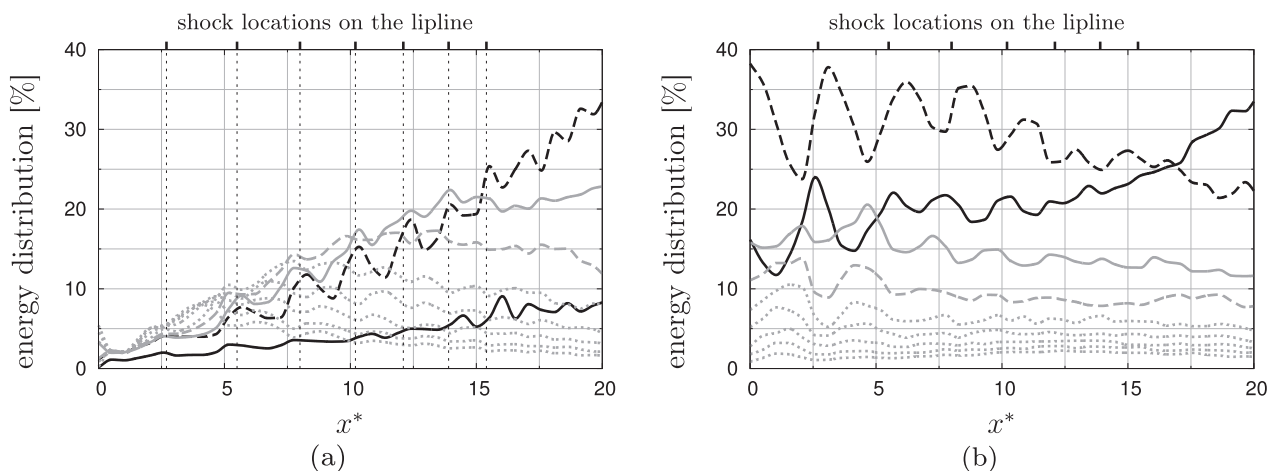
FIG. 22. Energy contribution of the first eight azimuthal modes of (a) the axial velocity along the lipline (array A) and (b) the pressure along array B. Black solid line: $m = 0$; black dashed line: $m = 1$; grey solid line: $m = 2$; grey dashed line: $m = 3$; grey dotted line: $4 \leq m \leq 8$.

and are discussed below. An azimuthal mode decomposition is performed on arrays A and B at each axial location. It consists in a double FFT in time and azimuth. The results are reported in Fig. 22 in terms of energy distribution between modes denoted as m. The axisymmetric mode corresponds to $m = 0$. The highest calculable mode is $m = 35$, i.e., the 36th mode, since the numerical arrays include 72 points in the azimuthal direction. The contribution of the first eight modes of the axial velocity on array A is depicted in Fig. 22(a). The shock locations in the shear layer are represented with vertical dotted lines. The initial contribution of modes $m \leq 4$ is negligible, and the major part of the energy (~90%) is equally distributed on higher modes, which are not all drawn. In the range $2 < x_* < 14$, modes 1, 2, and 3 become dominant, while mode 0 remains weak even downstream of the end of the potential core, as obtained by de Cacqueray et al.[34] or Liu et al.[53] The shock cell structure has an important impact on the azimuthal content. The shock locations seem to match with peaks of modes 1 and 2, and valleys of modes $m \geq 4$. It can be deduced that the shock cell structure favors particular modes which is consistent with observations of many authors studying the BBSAN in axisymmetric free jets, especially screech tones.[2,11,53] However, this analysis does not permit us to definitely conclude on the nature of the modes, i.e., flapping (mode B) or helical (mode C) which would require a treatment such as a proper orthogonal decomposition.

The contribution of the first eight modes of the pressure on array B is depicted in Fig. 22(b). Similar bumped shapes are found for the mode 1 in the range $0 < x_* < 12$, where it is dominant, at the expense of higher modes $m \geq 2$ which exhibit inverse bump patterns. It highlights the strong link between the mode 1 and the noise generation mechanisms in the shear layer in this region. The axisymmetric mode contribution starts to increase for $x_* > 12$ and becomes

predominant downstream for $x_* > 17$. Bogey and Bailly[68] have proposed a mechanism consisting in intermittent intrusions of vortical structures inside the end of the potential core. These structures are suddenly accelerated on the jet axis, exciting the acoustic azimuthal mode 0. Bogey and Bailly have suggested that it could be the major noise source radiating downstream at shallow angles in subsonic jets, but a similar mechanism can occur for supersonic jets, causing the dominant mode 0 observed at the downstream extremity of array B.

C. Pressure far field

1. Spatio-frequency content

The acoustic far field has been succinctly presented in Secs. III B 2 and III B 3 in terms of OASPL and PSDs at four observation angles for validation purposes. This section aims at providing extended results and analysis. The PSDs and the corresponding spectrogram of the pressure signal at the far field microphones are shown in Fig. 23. PSD peak frequencies are roughly distributed from $St = 0.02$ at a shallowest angle up to $St = 0.2$ on the sideline. The Mach wave radiation corresponds to the broadband high level region for $\theta' < 70°$ on the spectrogram. The BBSAN corresponds to the thinner band extending upstream for $\theta' > 90°$. The BBSAN peak frequency function of the observation angle θ' is plotted as blue dashed lines according to Eq. (22). It coincides with PSD peaks from $\theta' \gtrsim 90°$ and tends to $St_{BBSAN} = St_{up}$ upstream as expected. Such far field spectrogram patterns are similar to what has been obtained experimentally for analogous jets, by Schlinker et al.,[69] for example.

The Mach wave radiation and the BBSAN appear to be both easily identifiable in the far field regarding the PSDs peak frequency variation function of the observation angle. The peak frequency field depicted in Fig. 24(b) is obtained
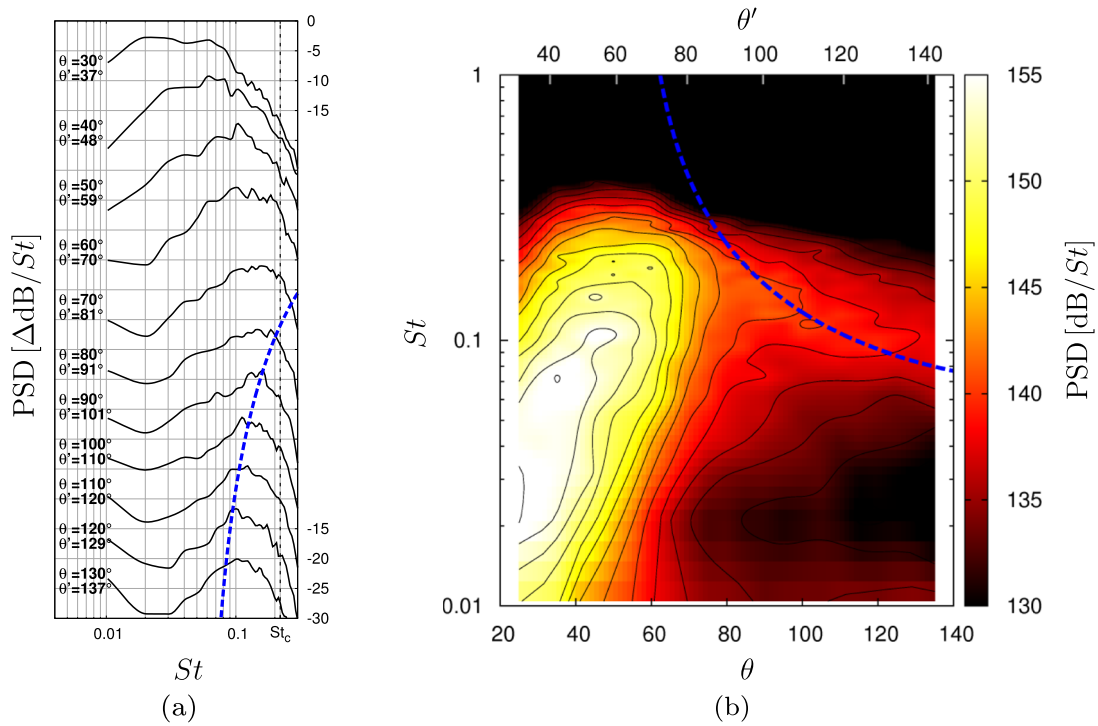
FIG. 23. PSDs of the pressure measured at far field microphone locations with (a) PSDs offset by 7 dB from others and (b) spectrogram function of θ. Black solid line: present numerical data; blue dashed line: $St = St_{BBSAN}(\theta')$; black line: PSD iso-lines every $\Delta 2$ dB/St.

by extracting the peak of the pressure PSD at each point of the mesh intersecting a 2D plane. It enables us to highlight more clearly main acoustic regions. In addition, the root mean square pressure field is shown in Fig. 24(a). The patterns appear to be roughly centered on the end of the potential core which justified the use of the transformed angle
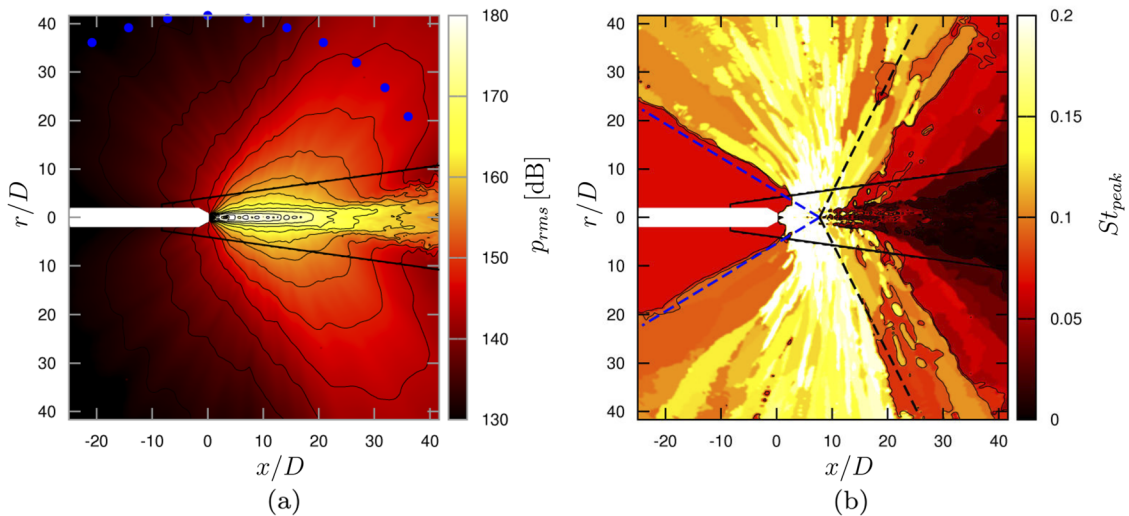
FIG. 24. (a) Pressure RMS level field and (b) spectrum central frequency field. Blue circles: far field microphones; black line: iso-p_{rms} and iso-frequencies $St = 0.02$, $St = St_{up}$, and $St = 0.09$; black solid line: coupling interface; black dashed line: $\theta' = \theta'_{max} = 70°$; blue dashed line: $\theta' = \theta''_{up} = 145°$.
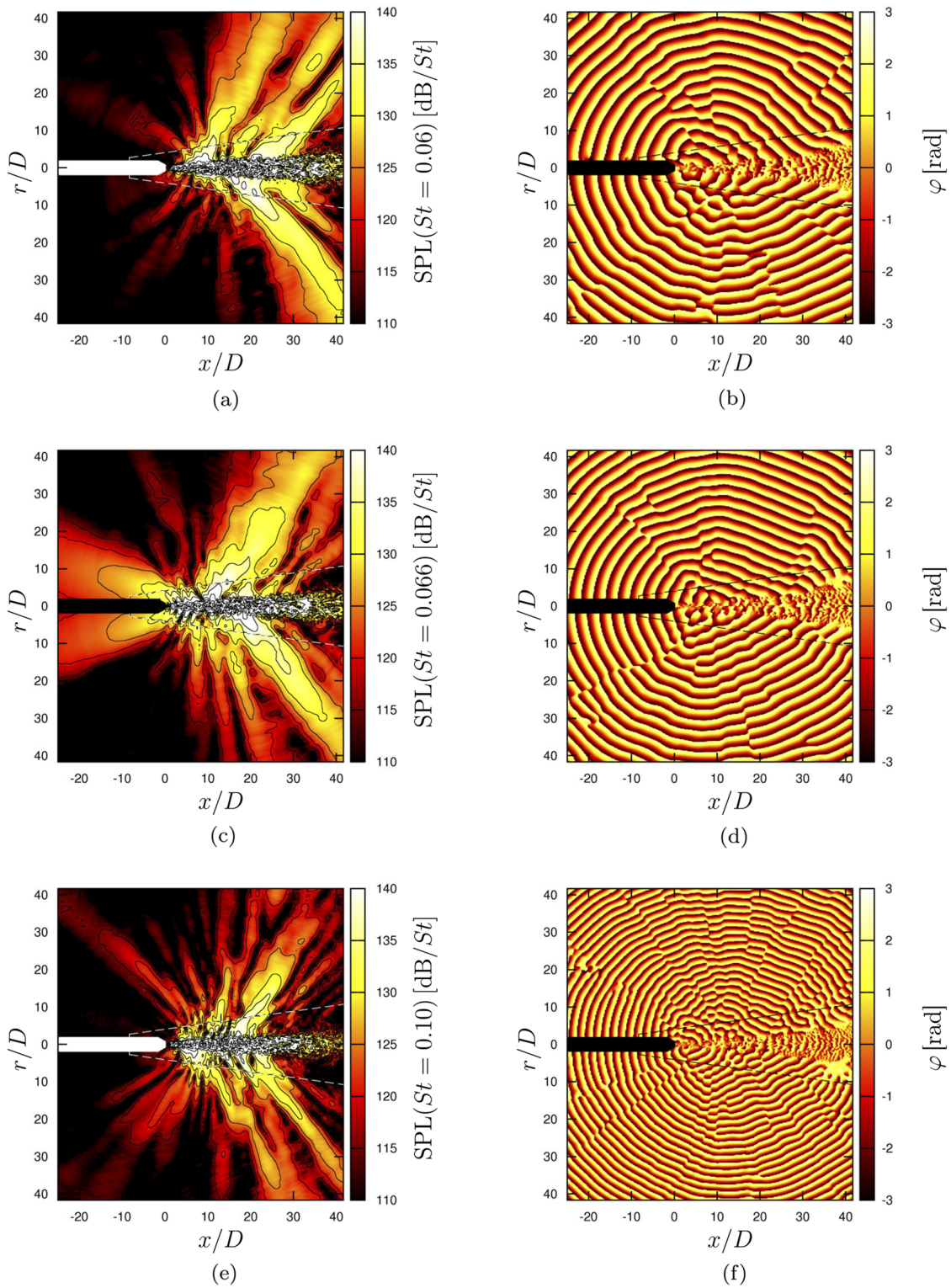
FIG. 25. Pressure RMS level fields and phase fields at three particular frequencies, [(a) and (b)] St = 0.060, [(c) and (d)] $St = St_{up}$ = 0.066, and [(e) and (f)] St = 0.100. Black line: iso-lines and black dashed line: coupling interface.

system. For angles $\theta' < 70°$ which corresponds to all possible Mach wave radiation angles ($\theta' < \theta'_{max}$), the noise is dominated by frequencies approximately in the range $0.01 < St < 0.1$. The very low peak frequencies observed at shallowest angles in the zone Z1 are due to slow flow events. At larger angles and especially close to the sideline at $\theta' \simeq 90°$, the noise is dominated by the BBSAN in mid frequencies up to the cut-off frequency $St_c = 0.22$. The peak frequency distribution is strongly inhomogeneous probably because of multiple source locations and interferences. More upstream, the BBSAN peak frequencies decrease due to the Doppler effect. From $\theta' \simeq 145°$, the distribution becomes strongly homogeneous at a peak frequency $St = St_{up}$. It cannot be fully explained by the BBSAN model discussed in Sec. IV A 2 since Eq. (22) yields $St_{BBSAN}(\theta' = 145) = 0.077 \neq St_{up}$. Tam[2] or Bailly and Fujii[3] have suggested that the instability wave interaction theory, from which Eq. (22) is derived, also predicts instability waves traveling in the upstream direction. These waves could generate Mach waves if their phase speeds c_φ are supersonic, i.e., if

$$c_\varphi < -c_\infty,$$
$$\frac{\omega}{\alpha - k_{shock}} < -c_\infty, \quad (23)$$

where $\omega = 2\pi f$, $\alpha \simeq \omega/u_c$, and $k_{shock} = 2\pi/D_j \overline{L^*_{shock}}$. Considering $\omega = 2\pi St_{up} u_j/D_j$, $u_c = 0.5 u_j$ ($M_{c\,3}$), and $\overline{L^*_{shock}} = 2.2$, this requirement is presently met and the Mach wave are consequently expected to radiate upstream at a very large angle $\theta' > 160°$ according to Eq. (18). It could explain the upstream dominant radiation at the frequency St_{up} and angles $\theta' > 160°$. However, these waves are also dominant in the range $145 < \theta' \leq 160°$ which is corroborated by the angle $\theta''_{up} = 145°$ found in Sec. IV B 1 analyzing the upstream radiation along array B. It can be related to the axial variation of u_c and L^*_{shock} and the associated uncertainties. According to Fig. 20(a), this Mach wave-like upstream BBSAN, denoted as MW-BBSAN in the following, has a lower intensity of about 15 dB compared to the standard downstream Mach waves.

The SPL and phase fields for three particular frequencies, including St_{up}, are shown in Fig. 25. The hypothesis of an upstream Mach wave radiation at the discrete frequency St_{up} (MW-BBSAN) is corroborated. Significant acoustic levels are indeed found upstream in Fig. 25(c), and the radiation is strongly directional around $\theta' = 155°$. Such patterns are not recovered for other frequencies in Fig. 25(a) ($St = 0.06$) and Fig. 25(e) ($St = 0.10$). Large bulbs corresponding to the standard Mach wave radiation are only found downstream. The multiple thinner bulbs mainly radiating in the sideline and upstream directions correspond to the BBSAN. The phase field in Fig. 25(d) clearly highlights that the upstream radiation at St_{up} is associated with the shock cell periodicity in the near field. The involved wave fronts are generated in opposition of phase in the cut plane, as also observed in Figs. 25(b) and 25(f). This observation is consistent with the azimuthal dominant mode 1 in the near field close to the strongest shocks [see Sec. IV B 2, Fig. 22(b)] and in the far field in the upstream direction [see Sec. IV C 2, Fig. 26(a)].
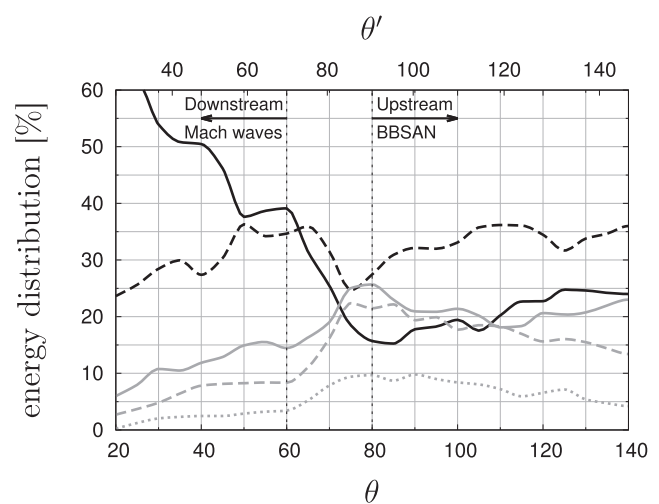

FIG. 26. Energy contribution of the first five azimuthal modes of the pressure at far field microphone location functions of θ and θ'. Black solid line: $m = 0$; black dashed line: $m = 1$; grey solid line: $m = 2$; grey dashed line: $m = 3$; grey dotted line: $m = 4$.

2. Azimuthal content

The contribution of the pressure azimuthal modes in the far field can be readily related to the acoustic near field. Figure 26 shows three angular regions with specific behaviors. Upstream at angles $\theta' > 90$, the noise is dominated by the BBSAN and azimuthal mode contributions are rather constant as a function of the angle. More than one third of the energy is included in mode 1 which can be associated with the mode 1 excited by the shock cell structure in the shear layer [Fig. 22(a)] and the strongly dominant mode 1 in the acoustic near field [Fig. 22(b)]. The range $70° < \theta' < 90°$, roughly the sideline direction, is a transition region between Mach waves and BBSAN. The contributions of modes 0 and 1 drop in favor of higher modes. This region can be associated with the inhomogeneous high peak frequencies in Fig. 24 discussed in Sec. IV C 1. Downstream at angles $\theta' < 70$, the noise is dominated by Mach waves essentially at mode 0. Mach waves radiating at the highest possible angles $60° < \theta' < 70°$ also contain an important mode 1 component. These waves are generated in the shear layer where the convection speed is maximum, i.e., before the end of the potential core [see Fig. 19(b)]. They are therefore probably highly perturbed by the shock cell structure. At shallower angles, the contribution of the axisymmetric mode strongly increases due to the intermittent intrusion of vortical structures inside the end of the potential core, as discussed in Sec. IV B 2.

D. Nonlinear propagation

1. Near field mechanism and cumulative effects

The acoustic nonlinear propagation is a key point of this study. Noise from a hot supersonic rocket plume involves nonlinear effects,[70] often associated with the crackle noise.[71]

However, the relative importance of local mechanisms in the near field and cumulative effects during propagation in the far field is still unclear. On the one hand, harsh flow events generating steep acoustic waveform directly emerging from the shear layer have been found to occur. This mechanism is known to be closely linked to the Mach wave radiation and is originally considered as the primary source of crackle. It has been observed experimentally[40] and reproduced numerically for supersonic jets by Nichols et al.[6] on a military-style configuration and more recently by Pineau and Bogey[72] using temporally developing jets, among the others. On the other hand, cumulative nonlinearities have been highlighted in the acoustic far field of supersonic jets by several authors, both experimentally[5,64] and numerically.[19,44] Such effects mainly consist in compression waves gradually steepening which is equivalent to a distortion of the probability density function of the signal, or in the frequency domain to an energy transfer from the peak to higher frequencies. Petitjean et al.[5] have found that $M_c > 1$ was a necessary condition for the onset of this kind of nonlinearity which is also a critical parameter for the Mach wave occurrence. As suggested in Fig. 19(b), this requirement is presently fulfilled on the lipline over a wide range of axial locations.

2. Metrics

The acoustic near and far fields are analyzed by focusing on the expected nonlinear effects. Specific metrics are introduced for this purpose, including the Goldberg number Γ, the skewness S [Eq. (8)], the kurtosis K [Eq. (9)], and the wave steepening factors WSF. The Goldberg number is defined by

$$\Gamma = \frac{\beta \omega p_{rms} \lambda}{\rho_\infty c_\infty^3 \alpha(\omega)}, \qquad (24)$$

where $\beta = (1+\gamma)/2$ is the nonlinearity coefficient and $\alpha(\omega)$ the dimensionless atmospheric damping function of the frequency, here estimated according to the standard ISO-9613.[51] It is assumed that $\Gamma < 1$ reflects a linear propagation and $\Gamma \gg 1$ reflects a nonlinear propagation.[7] The reference values for a Gaussian signal are $S = 0$ and $K = 3$. Note that compared to the raw pressure metrics $S(p)$ and $K(p)$, the pressure derivative metrics $S(\dot{p})$ and $K(\dot{p})$ are often considered as more sensitive and relevant to study nonlinear effects.[5,7,43] In both cases, S and K increase when the nonlinear effects are predominant over the atmospheric viscous damping. The WSF is defined as the modulus of the average negative slope divided by the average positive slope of the pressure waveform.[7,73] The reference value WSF = 1 corresponds to a pure harmonic waveform and WSF = 0 corresponds to a perfect sawtooth waveform. It decreases when the nonlinear effects are predominant over the atmospheric viscous damping. It can also be larger than 1 and theoretically tends to infinity in the case of discontinuous pressure drops. The evolution of these metrics for nonlinearly propagating waves has been studied, in particular, by Reichman et al.[43] (skewness) and Muhlestein et al.[73] (WSF), and experienced in many studies dealing with jet noise issues at various distances. Mora et al.[8] have found increasing
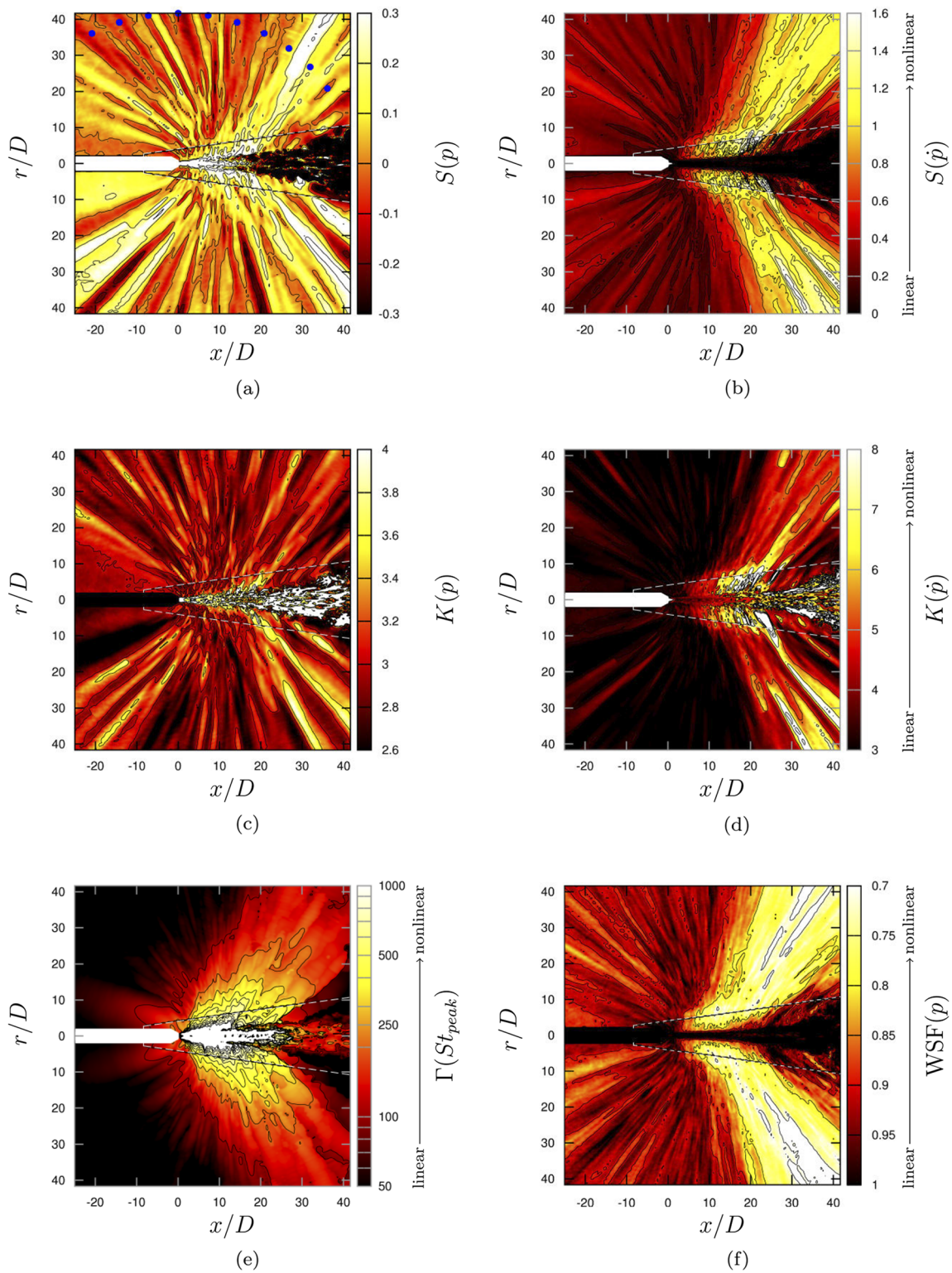
values of pressure derivative skewness and kurtosis up to $S(\dot{p}) > 0.8$ and $K(\dot{p}) > 4$ at a distance of about 25D from a $M > 1.5$ hot jet. Baars et al.[7,71] used the pressure derivative skewness and the WSF to identify cumulative nonlinearities out to 140D from a $M = 3$ cold jet in the peak noise direction. Schlinker et al.[69] have measured raw pressure skewness reaching values greater than 0.5 at an angle $\theta = 50°$ out to 300D from a $M > 1.5$ hot crackling jet.

The metrics mentioned above are plotted in Fig. 27 in a cut plane. The far field microphones are marked as blue dots in Fig. 27(a) for analysis convenience. The obtained skewness and kurtosis ranges are consistent with the values found by other authors at similar distances. The metrics based on the pressure time derivative clearly highlight the downstream Mach wave generation and radiation regions where nonlinear propagation effects are the most expected due to high acoustic levels. The metrics based on the raw pressure do not lead to such a result. All metrics indicate that strong nonlinearities also occur in the near field close to the shear layer. In particular, high excesses of $S(\dot{p})$, $K(\dot{p})$, and values of WSF larger than 1 are noticeable at $x \simeq 25D$, suggesting sharp pressure raises or drops. A similar behavior has been found for crackling jets, and it adds credit to a crackle generation mechanism located in the shear layer. On the other hand, most of the metrics are found to be still significantly varying in the far field out to 40D, especially WSF. It decreases to less than 0.6 in several locations associated with high levels of $S(\dot{p})$ and $K(\dot{p})$ which indicates that compression waves are still steepening due to the nonlinear propagation. It is consistent with the Goldberg number field which shows typical nonlinear values greater than 100 within two lobes extending in the far field in the peak direction.

3. Method relevancy

These metrics suggest that nonlinear effects can occur in both the near field and the far field. One could assume that far field nonlinear effects are negligible compared to near field events. This issue is handled by performing a linear Ffowcs Williams and Hawkings extrapolation from a cylindrical integration surface at a radius $r_{FWH} = 11.2D$ which is fully included in the Euler domain. The resulting acoustic levels at the far field microphones for $\theta \leq 100°$ are depicted in Fig. 28. The linear computation does not overestimate the levels, which is counter-intuitive regarding the Euler vs FWH comparison based on a previous flow solution[44] in Fig. 16. It could indicate that most of the nonlinear effects are included inside the cylinder of radius r_{FWH}.

However, the overall acoustic levels alone are definitely not conclusive about the method relevancy. The azimuthally averaged statistics of the pressure signal at two key locations in the far field are given in Table III. The numerical data from the far field microphones at $\theta = 40°$ and $\theta = 90°$ allow the comparison with the experimental data. As noted previously, the acoustic levels are similar but significant differences are found for the other metrics, including the peak Strouhal, $S(\dot{p})$, $K(\dot{s})$, and WSF. The Navier-Stokes-Euler computation fairly

FIG. 27. Nonlinearity metric maps including (a) raw pressure skewness, (b) pressure derivative skewness, (c) raw pressure kurtosis, (d) pressure derivative kurtosis, (e) Goldberg number at the peak frequency, and (f) wave steepening factor. Blue circles: far field microphones; black line: iso-lines; black dashed line: coupling interface.
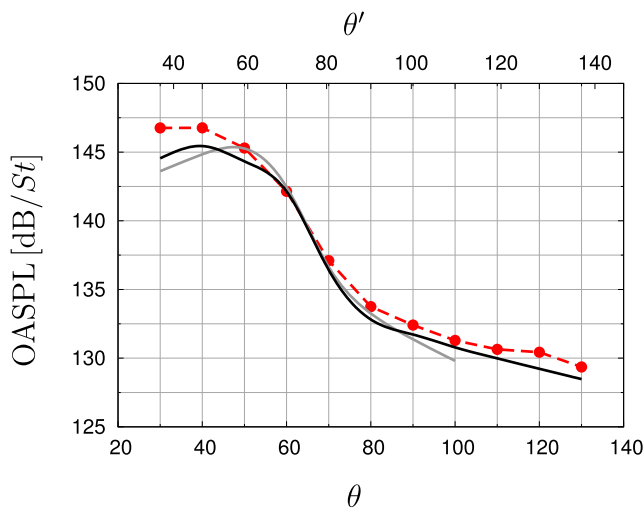
FIG. 28. OASPL at the far field microphones computed by integrating the PSDs over the range $0.01 \leq St \leq 0.22$. Red dotted dashed line: experimental data; black solid line: NS-Euler computation; grey solid line: NS-Euler-FWH computation.

agrees with the experimental data at the two angles. In particular, significantly higher values of $S(\dot{p})$ and lower values of WSF are found as expected in the case of a nonlinear

propagation. An extended analysis is proposed with Fig. 29. The derivative skewness, kurtosis, and the steepening factor calculated from both the experimental and the numerical signals are plotted against the observation angle. The Navier-Stokes-Euler computation provides consistent results with respect to the experiment and clearly demonstrates its ability to take into account nonlinear effects with peak values around the peak direction $\theta' = 48°$. Such trends are not well recovered by the Ffowcs Williams and Hawkings approach.

Furthermore, the metric $K(\dot{s})$ presents the higher measurement dynamic but also the larger discrepancies between the experiment and the Navier-Stokes-Euler computation, and the lower discrepancies between the Euler and the Ffowcs Williams and Hawkings computations. The metrics $S(\dot{p})$ and WSF appear to be more robust in quantifying cumulative nonlinearities. $S(\dot{p})$ typically remains below 1.5 in the Navier-Stokes-Euler computation at a distance of 40D from the sources, while the experimental data show a peak $S(\dot{p}) > 1.75$. Reichman et al.[43] have associated shocked waveform appearance with values greater than 1.5 which suggests that shocks exist in experiments but are not properly captured in the computation. It highlights a major limitation of the Navier-Stokes-Euler computation. The cut-off frequency $St_c = 0.22$ seems too low to fully reproduce the nonlinear phenomena.

TABLE III. Azimuthally averaged statistics of the pressure signal from the NS-Euler-FWH computation, NS-Euler computation, and the experiment at the far field microphones $\theta = 90°$ and $40°$.

θ	θ'	Method	p_{rms} (dB)	St_{peak}	$S(p)$	$S(\dot{p})$	$K(p)$	$K(\dot{p})$	WSF
90°	101°	NS-Euler-FWH	131.4	0.258	+0.09	−0.02	2.98	3.39	1.00
		NS-Euler	131.7	0.154	−0.03	+0.25	2.96	2.90	0.94
		Experimental	132.5	0.176	+0.29	+0.45	3.24	3.64	0.89
40°	48°	NS-Euler-FWH	144.8	0.064	−0.05	−0.04	2.59	4.06	1.00
		NS-Euler	145.5	0.066	+0.09	+1.21	3.04	5.50	0.73
		Experimental	146.8	0.072	+0.60	+1.79	3.72	9.79	0.68

(a)　　　　　　　　(b)　　　　　　　　(c)
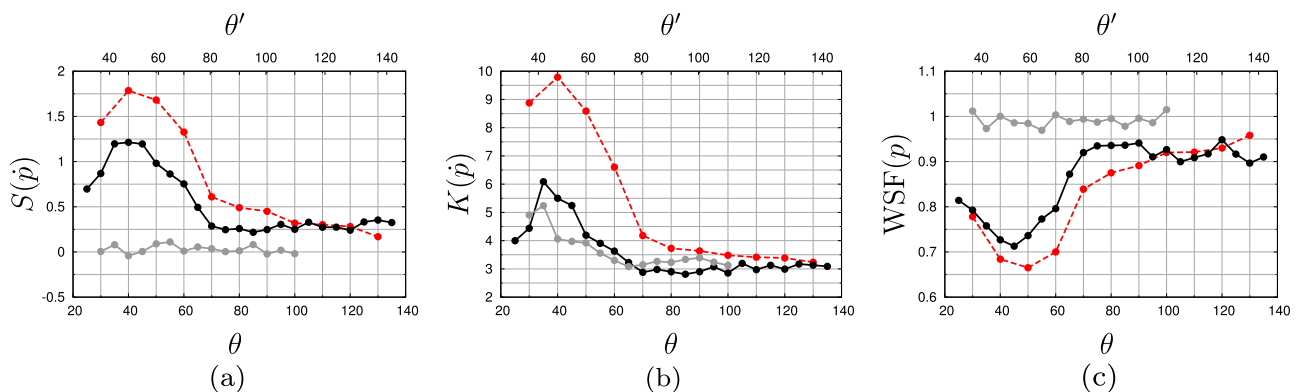
FIG. 29. Azimuthally averaged $S(\dot{p})$, $K(\dot{s})$, and WSF metric function of θ and θ'. Red dotted dashed line: experimental data; black dotted solid line: NS-Euler computation; grey dotted solid line: NS-Euler-FWH computation.

V. CONCLUSION

A numerical methodology including a two-way Navier-Stokes-Euler coupling, a geometrical turbulence tripping, and a high-order nonlinear acoustic solver is described and applied to the simulation of a hot M = 3.1 supersonic jet. The jet parameters correspond to an experiment conducted at the MARTEL facility which aims at investigating the acoustic field during the launcher lift-off. The turbulence tripping method using a small step in the nozzle convergent associated with an important effort on the mesh refinement leads to a major improvement of the flow solution compared to previous studies. This approach enables us to get velocity fluctuation levels greater than 2% in the nozzle divergent. A highly disturbed exit condition is thereby obtained at the nozzle lips.

The aerodynamic near field and the acoustic far field fairly agree with the available experimental data. In particular, the shear layer development shows proper features in terms of spread rate, velocity fluctuation levels, and turbulent spectra. The far field acoustic levels are recovered within a 1 dB error at most of observation angles, and the spectra are well predicted in all directions despite a slight underestimation at shallowest angles. Based on these results, an extended physical analysis of the radiated noise is performed. The acoustic near and far fields are consistent with the noise generation mechanisms described and modeled in the literature. The noise is generated via two main mechanisms: the Mach wave radiation essentially downstream and the broadband shock-associated noise essentially upstream.

The Mach wave radiation angles are related to the convection speed of large turbulent structures. In the range $2 < x_* < 12$ along the lipline, where $x_* = x/D_j$, this convection speed is maximum leading to Mach wave emission expected at angles $60° < \theta' < 70°$. The resulting noise is broadband centered on mid frequencies $St \simeq 0.1$ and contains an important $m = 1$ azimuthal component attributed to the velocity mode 1 in the shear layer. Downstream of the end of the potential core, the convection velocity in the shear layer decreases, leading to Mach waves radiating at angles $40° < \theta' < 60°$. An additional mechanism, consisting in the intermittent intrusions of vortical structures inside the end of the potential core and convected on the centerline, can explain the low frequency noise strongly dominated by the azimuthal mode 0 at shallower angles. From these conclusions, one can also deduce that the noise sources associated with large turbulent structures are broadly axially distributed.

Close to the sideline direction for angles $70° < \theta' < 90°$, the main noise source is not well defined. This angle range is considered as a transition region. The noise is broadband centered on mid frequencies $St > 0.1$ with an important contribution of azimuthal modes $1 \le m \le 3$. In the upstream direction for angles $90° < \theta' < 145°$, the shock-associated noise mechanism generates broadband spectra centered on a frequency St_{BBSAN} function of the angle. This frequency in the simulation agrees with the experimental data and with Tam and Tanna's model. The azimuthal decomposition of the broadband shock-associated noise is dominated by the mode 1 in all upstream directions which is attributed to the excited mode 1 of the velocity in the shear layer. A particular shock-associated noise source radiating through a Mach wave-like mechanism is highlighted at large angles $\theta' > 145°$. This noise component presents a bump corresponding to the screech frequency, although the present jet is not screeching as expected for such a hot jet.

Finally, nonlinear effects are investigated. Both near and far field phenomena are highlighted. On the one hand, sharp pressure drops and raises are found in the vicinity of the shear layer which could correspond to the near field generation mechanism of crackle noise. On the other hand, the high acoustic levels clearly result in cumulative nonlinear effects in the far field, especially the peak direction, as suggested by the pressure derivative skewness or the wave steepening factor metrics. It justifies the use of a nonlinear acoustic solver.

APPENDIX: PARAMETRIC STUDY FOR THE GEOMETRICAL TRIPPING

A short parametric study is conducted by varying the step main parameters, i.e., the axial location x^*_{step}, the height h_*, and the top edge slope, as sketched in Fig. 30. Five configurations have been investigated, and the corresponding parameters are given in Table IV. The steps A, B, and C are located in the convergent, the step D is located in the divergent, and a configuration without step is used as a reference. The nozzle geometry and the generating conditions are the same as for the full case. The free field domain downstream of the nozzle exit is, however, downsized and coarsened for computational cost reasons. The ambient pressure is slightly diminished compared to the nominal parameter p_∞ to prevent any wall flow separation phenomenon which may occur for overexpanded exit conditions. The mesh characteristics in the nozzle are set to those provided in Table II for all configurations, except in the vicinity of the step when it exists, in order to quantify the tripping effects independently of the grid refinement. The vicinity of the step is discretized with tetrahedral elements connected to the hexahedral wall elements which explains the size drop at $x^* = x^*_{step}$ in Fig. 2 and the important penalty in terms of cell number reported in Table IV.

The velocity fluctuations normalized by the jet exit velocity $\sqrt{(u'^2_x + u'^2_r + u'^2_\Theta)}/u_j$ recorded along the wall and within the
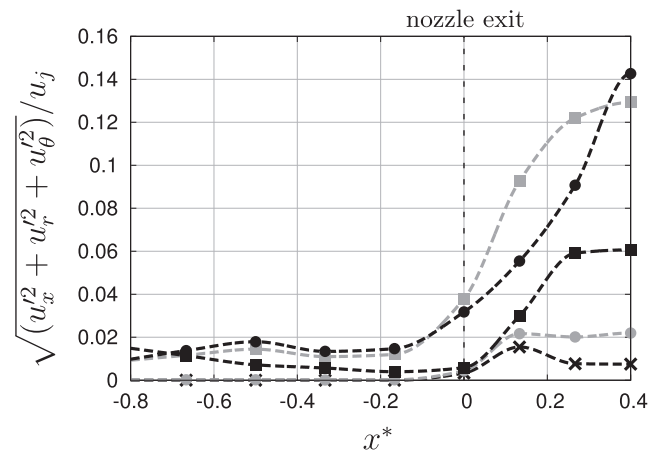
(a)

(b)
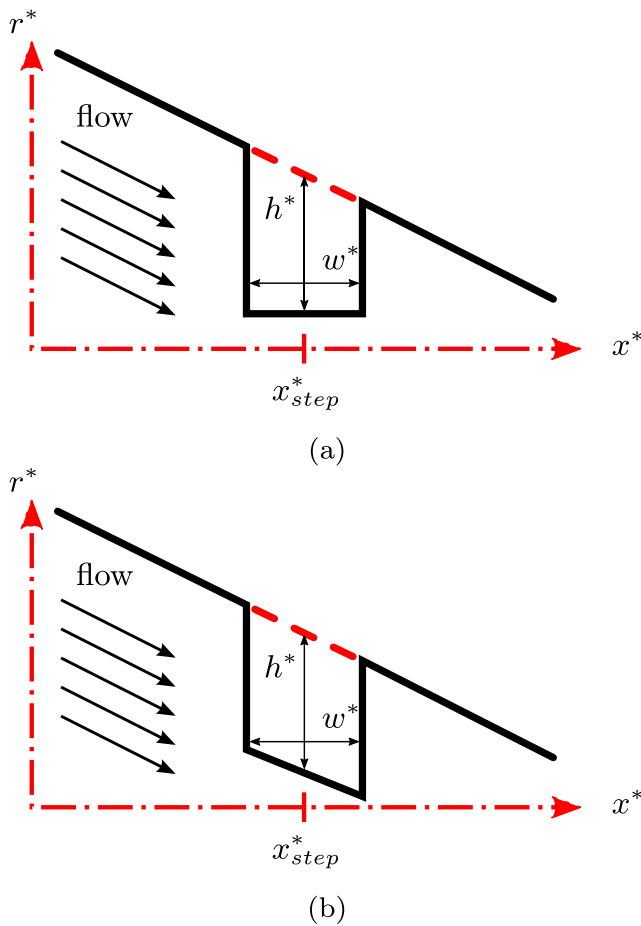
FIG. 30. Nozzle step configurations with a step edge slope (a) parallel to $\vec{x}$ or (b) parallel to the wall.

FIG. 31. Fluctuating velocity intensity in the nozzle boundary layer and the free jet initial shear layer. Black crossed dashed line: without step; grey dotted dashed line: step A; grey square dashed line: step B; black dotted dashed line: step C; black square dashed line: step D.

the divergent for a supersonic nozzle. The step strongly disturbs the whole flow because of the additional attached and reflected shocks downstream. It is chosen to implement the step C in the full computation since it leads to the highest fluctuation levels.

initial shear layer are shown in Fig. 31. The step height appears to have a major impact. The step A ($h_* = 0.6\%$) provides similar fluctuation levels to the step-free configurations, i.e., less than 0.5% at the nozzle lips, while the steps B and C ($h_* = 1\%$) reach more than 3%. The top edge slope modifies the wake flow but seems to have a limited influence on the levels inside the nozzle and slightly changes the growth rate downstream. The step D provides higher fluctuation levels than the reference, but this configuration illustrates that the trip cannot be placed in

TABLE IV. Step parameters in the parametric study.

Step	Zone	x^*_{step}	h_*	w_*	Slope	Mesh size
None	...	...	0.0	...	...	29.4×10^6
A	Convergent	−1.38	0.006	0.007	// wall	37.9×10^6
B	Convergent	−1.38	0.010	0.007	// wall	40.7×10^6
C	Convergent	−1.38	0.010	0.007	// $\vec{x}$	42.2×10^6
D	Divergent	−1.08	0.006	0.006	// $\vec{x}$	47.9×10^6

REFERENCES

[1] B. Chemoul, E. Louaas, P. Roux, D. Schmitt, and M. Pourcher, "Ariane 5 flight environments," Acta Astronaut. **48**, 275–285 (2001).

[2] C. Tam, "Supersonic jet noise," Annu. Rev. Fluid Mech. **27**, 17–43 (1995).

[3] C. Bailly and K. Fujii, "High-speed jet noise," Mech. Eng. Rev. **3**, 15-00496 (2016).

[4] C. Tam, K. Viswanathan, K. Ahuja, and J. Panda, "The source of jet noise: Experimental evidence," J. Fluid Mech. **615**, 253–292 (2008).

[5] B. Petitjean, K. Viswanathan, and D. McLaughlin, "Acoustic pressure waveforms measured in high speed jet noise experiencing nonlinear propagation," AIAA J. **5**, 193–215 (2006).

[6] J. Nichols, S. Lele, F. Ham, S. Martens, and J. Spyropoulos, "Crackle noise in heated supersonic jets," J. Eng. Gas Turbines Power **135**, 051202 (2013).

[7] W. Baars, C. Tinney, M. Wochner, and M. Hamilton, "On cumulative nonlinear acoustic wave distortions from high-speed jets," J. Fluid Mech. **749**, 331–366 (2014).

[8] P. Mora, J. Kastner, and E. Gutmark, "Impact of heat on the pressure skewness and kurtosis in supersonic jets," AIAA J. **52**, 777–787 (2014).

[9] J. Panda, "Shock oscillation in underexpanded screeching jets," J. Fluid Mech. **363**, 173–198 (1998).

[10] A. Krothapalli, E. Rajkuperan, F. Alvi, and L. Lourenco, "Flow field and noise characteristics of a supersonic impinging jet," J. Fluid Mech. **392**, 155–181 (1999).

[11] D. Edgington-Mitchell, K. Oberleithner, D. Honnery, and J. Soria, "Coherent structure and sound production in the helical mode of a screeching axisymmetric jet," J. Fluid Mech. **748**, 822–847 (2014).

[12] T. Ishii, S. Tsutsumi, K. Ui, S. Tokudome, Y. Ishii, K. Wada, and S. Nakamura, "Acoustic measurement of 1 : 42 scale booster and launch pad," *164th Meeting of the Acoustical Society of America* (ASA, Kansas City, MO, USA, 2012), Vol. 18, pp. 1–13.

[13]D. Munday, N. Heeb, and E. Gutmark, "Acoustic effects of chevrons on supersonic jets exiting conical convergent-divergent nozzles," AIAA J. **50**, 2336–2350 (2012).

[14]W. Horne, N. Burnside, J. Panda, and C. Brodell, "Measurements of unsteady pressure fluctuations in the near-field of a solid rocket motor plume," Int. J. Aeroacoust. **15**, 554–569 (2016).

[15]J. Varnier, V. Koudriavtsev, and A. Safronov, "Simplified approach of jet aerodynamics with a view to acoustics," AIAA J. **44**, 1690–1693 (2006).

[16]T. Nonomura and K. Fujii, "Overexpansion effects on characteristics of Mach waves from a supersonic cold jet," AIAA J. **49**, 2282–2294 (2011).

[17]R. Gojon, C. Bogey, and O. Marsden, "Investigation of tone generation in ideally expanded supersonic planar impinging jets using large-eddy simulation," J. Fluid Mech. **808**, 90–115 (2016).

[18]C. Bogey and R. Gojon, "Feedback loop and upwind-propagating waves in ideally expanded supersonic impinging round jets," J. Fluid Mech. **823**, 562–591 (2017).

[19]N. de Cacqueray and C. Bogey, "Noise of an overexpanded Mach 3.3 jet: Non-linear propagation effects and correlations with flows," Int. J. Aeroacoust. **13**, 607–632 (2014).

[20]G. Brès, F. Ham, J. Nichols, and S. Lele, "Unstructured large-eddy simulations of supersonic jets," AIAA J. **55**, 1164–1184 (2017).

[21]C. Bogey, O. Marsden, and C. Bailly, "Influence of initial turbulence level on the flow and sound fields of a subsonic jet at a diameter-based Reynolds number of 10^5," J. Fluid Mech. **701**, 352–385 (2012).

[22]J. Liu, K. Kailasanath, J. Boris, N. Heeb, D. Munday, and E. Gutmark, "Effect of the initial turbulence level on an underexpanded supersonic jet," AIAA J. **51**, 741–744 (2013).

[23]M. Lorteau, F. Cléro, and F. Vuillot, "Analysis of noise radiation mechanism in hot subsonic jet from a validated large eddy simulation solution," Phys. Fluids **27**, 075108 (2015).

[24]G. Brès, P. Jordan, V. Jaunet, M. Le Rallic, A. Cavalieri, A. Towne, S. Lele, T. Colonius, and O. Schmidt, "Importance of the nozzle-exit boundary-layer state in subsonic turbulent jets," J. Fluid Mech. **851**, 83–124 (2018).

[25]D. Long, T. McDonald, and P. Maye, "Effect of inlet flow conditions on noise and performance of supersonic nozzles," in 16th AIAA/CEAS Aeroacoustics Conference, 2010-3920, Stockholm, Sweden, 2010.

[26]A. Hussain and M. Zedan, "Effects of the initial condition on the axisymmetric free shear layer: Effect of the initial fluctuation level," Phys. Fluids **21**, 1475–1481 (1978).

[27]R. Fontaine, G. Elliott, J. Austin, and J. Freund, "Very near-nozzle shear-layer turbulence and jet noise," J. Fluid Mech. **770**, 27–51 (2015).

[28]C. Bogey and O. Marsden, "Identification of the effects of the nozzle-exit boundary-layer thickness and its corresponding Reynolds number in initially highly disturbed subsonic jets," Phys. Fluids **25**, 055106 (2013).

[29]M. Gloor, S. Buhler, and L. Kleiser, "Transition to turbulence and noise radiation in heated coaxial jet flows," Phys. Fluids **28**, 044103 (2016).

[30]C. Bogey, O. Marsden, and C. Bailly, "Large-eddy simulation of the flow and acoustic fields of a Reynolds number 10^5 subsonic jet with tripped exit boundary layers," Phys. Fluids **23**, 035104 (2011).

[31]G. Rahier, J. Prieur, F. Vuillot, N. Lupoglazoff, and A. Biancherin, "Investigation of integral surface formulations for acoustic post-processing of unsteady aerodynamic jet simulations," Aerosp. Sci. Technol. **8**, 453–467 (2004).

[32]G. Djambazov, C.-H. Lai, and K. Pericleous, "On the coupling of Navier-Stokes and linearized Euler equations for aeroacoustic simulation," Comput. Visualization Sci. **3**, 9–12 (2000).

[33]C. Bogey, S. Barré, D. Juvé, and C. Bailly, "Simulation of a hot coaxial jet: Direct noise prediction and flow-acoustics correlations," Phys. Fluids **21**, 035105 (2009).

[34]N. de Cacqueray, C. Bogey, and C. Bailly, "Investigation of a high-Mach-number overexpanded jet using large-eddy simulation," AIAA J. **49**, 2171–2182 (2011).

[35]R. Harris, E. Collins, E. Luke, A. Sescu, L. Strutzenberg, and J. West, "Hybrid discontinuous Galerkin and finite volume method for launch environment acoustics prediction," AIAA J. **53**, 3430–3447 (2015).

[36]R. Harris, E. Collins, E. Luke, and A. Sescu, "Coupled overset unstructured discontinuous Galerkin method for launch environment acoustics prediction," AIAA J. **54**, 1932–1952 (2016).

[37]O. Labbé, C. Peyret, G. Rahier, and M. Huet, "A CFD/CAA coupling method applied to jet noise prediction," Comput. Fluids **86**, 1–13 (2013).

[38]S. Tsutsumi, S. Ishii, K. Ui, S. Tokudome, and K. Wada, "Assessing prediction and reduction technique of lift-off acoustics using epsilon flight data," in 53rd AIAA Aerospace Sciences Meeting, 2015-1007, Kissimmee, FL, USA, 2015.

[39]A. Langenais, F. Vuillot, C. Peyret, G. Chaineray, and C. Bailly, "Assessment of a two-way coupling methodology between a flow and a high-order non-linear acoustic unstructured solvers," Flow, Turbul. Combust. **101**, 681–703 (2018).

[40]A. Krothapalli, L. Venkatakrishnan, and L. Lourenco, "Crackle: A dominant component of supersonic jet mixing noise," 6th AIAA/CEAS Aeroacoustics Conference, 2000-2024, Lahaina, HI, USA, 2000.

[41]M. Shepherd, K. Gee, and M. Wochner, "Short-range shock formation and coalescence in numerical simulation of broadband noise propagation," J. Acoust. Soc. Am. **126**, 2886–2893 (2009).

[42]M. Muhlestein, K. Gee, T. Neilsen, and D. Thomas, "Prediction of nonlinear propagation of noise from a solid rocket motor," in 164*th Meeting of the Acoustical Society of America* (ASA, 2012), Vol. 18.

[43]B. Reichman, M. Muhlestein, K. Gee, T. Neilsen, and D. Thomas, "Evolution of the derivative skewness for nonlinearly propagating waves," J. Acoust. Soc. Am. **139**, 1390–1403 (2016).

[44]A. Langenais, F. Vuillot, J. Troyes, and C. Bailly, "Numerical investigation of the noise generated by a rocket engine at lift-off conditions using a two-way coupled CFD-CAA method." in 23rd AIAA/CEAS Aeroacoustics Conference, 2017-3212, Denver, CO, USA, 2017.

[45]J. Troyes, F. Vuillot, H. Lambaré, and A. Espinosa Ramos, "Numerical study of free supersonic hot jet on unstructured grids with emphasis on aerodynamics and resulting radiated noise," in 22nd AIAA/CEAS Aeroacoustics Conference, 2016-2734, Lyon, France, 2016.

[46]C. Hirsch, *Numerical Computation of Internal and External Flows*, Volume 2: Computational Methods for Inviscid and Viscous Flows (John Wiley & Sons, 1990), ISBN: 978-0471924524.

[47]A. Refloch, B. Courbet, A. Murrone, P. Villedieu, C. Laurent, P. Gilbank, J. Troyes, L. Tessé, G. Chaineray, J.-B. Dargaud, E. Quémerais, and F. Vuillot, "CEDRE software," Aerospace Lab J. **2**, AL02-11 (2011).

[48]P. Delorme, P. Mazet, C. Peyret, and Y. Ventribout, "Computational aeroacoustics applications based on a discontinuous Galerkin method," C. R. Mec. **333**, 676–682 (2005).

[49]R. Léger, C. Peyret, and S. Piperno, "Coupled discontinuous Galerkin/finite difference solver on hybrid meshes for computational aeroacoustics," AIAA J. **50**, 338–349 (2012).

[50]C. Tam, "Computational aeroacoustics: Issues and methods," AIAA J. **33**, 1788–1796 (1995).

[51]ISO 9613-1:1993–Acoustics–Attenuation of Sound During Propagation outdoors–Part 1: Air Absorption, 1993.

[52]E. Quémerais, Coupling with interpolation parallel interface, ONERA web site (2016).

[53]J. Liu, A. Corrigan, K. Kailasanath, R. Ramamurti, and E. Gutmark, "Helical screech tone generation in overexpanded jets," in 23rd AIAA/CEAS Aeroacoustics Conference, 2017-3208, Denver, CO, USA, 2017.

[54]R. Narasimha and K. Sreenivasan, "Relaminarization of fluid flows," Adv. Appl. Mech. **19**, 221–309 (1979).

[55]E. Morrisette and T. Goldberg, "Turbulent-flow Separation Criteria for Overexpanded Supersonic Nozzles," Technical Paper No. 1207 (NASA, Hampton, VA, USA, 1978).

[56] H. Schlichting and K. Gersyen, *Boundary-layer Theory*, 7th ed. (Springer, 1979), ISBN: 978-3662529171.

[57] T. Maeder, N. Adams, and L. Kleiser, "Direct simulation of turbulent supersonic boundary layers by an extended temporal approach," J. Fluid Mech. **429**, 187–216 (2001).

[58] L. Jacquin, S. Mistral, P. Geffroy, and F. Cruand, "Mixing of a heated supersonic jet with a supersonic parallel stream," 5th European Turbulence Conference, Siena, Italy, 1994.

[59] C. Tam and H. Tanna, "Shock-associated noise of supersonic jets from convergent-divergent nozzles," J. Sound Vib. **81**, 337–358 (1982).

[60] C. Tam, S. Parrish, and K. Viswanathan, "Harmonics of jet screech tones," AIAA J. **52**, 2471–2479 (2014).

[61] T. Troutt and D. McLaughlin, "Experiments on the flow and acoustic properties of a moderate-Reynolds-number supersonic jet," J. Fluid Mech. **116**, 123–156 (1982).

[62] B. Greska, A. Krothapalli, W. Horne, and N. Burnside, "A near-field study of high temperature supersonic jets," in 14th AIAA/CEAS Aeroacoustics Conference, 2008-3026, Canada, Vancouver, 2008.

[63] S. Lele and J. Larsson, "Shock-turbulence interaction: What we know and what we can learn from peta-scale simulations," J. Phys.: Conf. Ser. **180**, 012032 (2009).

[64] K. Gee, V. Sparrow, M. James, J. Downing, C. Hobbs, T. Gabrielson, and A. Atchley, "The role of nonlinear effects in the propagation of noise from high-power jet aircraft," J. Acoust. Soc. Am. **123**, 4082–4093 (2008).

[65] A. Vaughn, T. Neilsen, K. Gee, A. Wall, J. Downing, and M. James, "Broadband shock-associated noise from a high-performance military aircraft," J. Acoust. Soc. Am. **144**, EL242–EL247 (2018).

[66] H. Oertel, F. Seiler, J. Srulijes, and R. Hruschka, "Mach waves produced in the supersonic jet mixing layer by shock/vortex interaction," Shock Waves **26**, 231–240 (2016).

[67] J. Panda and R. Seasholtz, "Experimental investigation of density fluctuations in high-speed jets and correlation with generated noise," J. Fluid Mech. **450**, 97–130 (2002).

[68] C. Bogey and C. Bailly, "An analysis of the correlations between the turbulent flow and the sound pressure field of subsonic jets," J. Fluid Mech. **583**, 71–97 (2007).

[69] R. Schlinker, S. Liljenberg, D. Polak, K. Post, C. Chipman, and A. Stern, "Supersonic jet noise source characteristics & propagation: Engine and model scale," in 13th AIAA/CEAS Aeroacoustics Conference, 2007-3623, Rome, Italy, 2007.

[70] S. McInerny, "Launch vehicle acoustics part II: Statistics of the time domain data," J. Aircr. **33**, 518–523 (1996).

[71] W. Baars and C. Tinney, "Shock-structures in the acoustic field of a Mach 3 jet with crackle," J. Sound Vib. **333**, 2539–2553 (2014).

[72] P. Pineau and C. Bogey, "Numerical study of the sound fields of temporally-developing supersonic round jets," in 23rd AIAA/CEAS Aeroacoustics Conference, 2017-3209, Denver, CO, USA, 2017.

[73] M. Muhlestein, K. L. Gee, T. Neilsen, and D. Thomas, "Evolution of the average steepening factor for nonlinearly propagating waves," J. Acoust. Soc. Am. **137**, 640–650 (2015).